Ciliary central apparatus structure reveals mechanisms of microtubule patterning

Miao Gui[1], **Xiangli Wang**[2], **Susan K. Dutcher**[3], **Alan Brown**[1,*], **Rui Zhang**[2,*]

[1]Department of Biological Chemistry and Molecular Pharmacology, Blavatnik Institute, Harvard Medical School, 240 Longwood Avenue, Boston, MA, USA.

[2]Department of Biochemistry and Molecular Biophysics, Washington University in St. Louis, School of Medicine, St. Louis, MO, USA.

[3]Department of Genetics, Washington University in St. Louis, St Louis, MO, USA.

Abstract

A pair of extensively modified microtubules form the central apparatus (CA) of the axoneme of most motile cilia, where they regulate ciliary motility. The external surfaces of both CA microtubules are patterned asymmetrically with large protein complexes that repeat every 16 or 32 nm. The composition of these projections and the mechanisms that establish asymmetry and longitudinal periodicity are unknown. Here, by determining cryo-EM structures of the CA microtubules, we identify 48 different CA-associated proteins, which in turn reveal mechanisms for asymmetric and periodic protein binding to microtubules. We identify arc-MIPs, a novel class of microtubule inner protein that bind laterally across protofilaments and remodel tubulin structure and lattice contacts. The binding mechanisms utilized by CA proteins may be generalizable to other microtubule-associated proteins. These structures establish a foundation to elucidate the contributions of individual CA proteins to ciliary motility and ciliopathies.

Introduction

The central apparatus (CA) of motile cilia consists of a pair of singlet microtubules, C1 and C2, which are decorated by structurally distinct projections of interconnected complexes that repeat with either 16- or 32-nm longitudinal periodicity[1]. In *Chlamydomonas reinhardtii*, a biflagellate alga and model organism for understanding the atomic structure of the axoneme[2–4], there are six projections on the C1 microtubule (C1a-e) and five on the C2 microtubule (C2a-f)[5]. The mammalian CA is morphologically similar but lacks the

C1f projection[6]. The projections interact with radial spoke complexes that radiate inwards from doublet microtubules surrounding the CA (Fig. 1a) to regulate ciliary motility[7]. Over 60 *Chlamydomonas* proteins have been assigned to the CA using comparative mutant studies and proteomics[8–12]. Despite this comprehensive parts list, the spatial organization, interactions, and functions of these projections are poorly understood. It is also unknown what directs individual projections to specific microtubules or protofilaments, and what defines their periodicities.

The absence of the CA or its projections paralyzes cilia or causes them to beat slowly or with abnormal waveforms[13,14]. In humans, this disruption of ciliary motility manifests as motile ciliopathies. Mutations in the genes encoding the CA proteins CFAP221[15], HYDIN[16], and SPEF2[17] are causatively associated with primary ciliary dyskinesia (PCD), a disease characterized by impaired mucociliary clearance and immotile spermatozoa, whereas mutations of other CA genes (including *CFAP47*[18] and *CFAP69*[19]) are associated with multiple morphological abnormalities of sperm flagella (MMAF) with little apparent effect on respiratory cilia. Structural information is essential to understand the molecular assemblies that form the CA, their roles in regulating ciliary motility, and how their mutations contribute to human ciliopathies.

Results

Structure determination

To obtain structural information for the CA we biochemically dissociated *Chlamydomonas* axonemes into singlet and doublet microtubules for single-particle cryo-EM imaging[2]. From the micrographs, we manually selected isolated singlet CA microtubules and those that occur in loosely associated pairs (Extended Data Fig. 1a,b) and used *in silico* supervised classification to determine individual structures of the C1 and C2 microtubules (Fig. 1 and Table 1). Both microtubules have 13 protofilaments with seams that face each other at the bridge that connects them. The structures show that all projections on the C1 microtubule have survived purification, whereas projections C2b-d and elements at the bridge have been lost or are substoichiometric (Fig. 1b). Using a combination of protein-identification strategies (Methods and Extended Data Fig. 2), we identified 36 proteins in the C1 microtubule and 14 proteins in the C2 microtubule. These proteins are listed in Supplementary Table 1 and their positions mapped onto the CA projections in Extended Data Fig. 3a. The stoichiometries and periodicities of the proteins within the CA vary greatly and copies of the same protein can be found in more than one location on the same microtubule (for example, the catalytic subunit of Protein phosphatase 1 (PP1c) is found in both the C1d and C1e projections; Extended Data Fig. 3b) or on different microtubules (FAP174 and FAP236). Some proteins (e.g., Hydin and FAP47) may even span C1 and C2 microtubules (see later). The domain organization of all identified proteins is provided in Extended Data Fig. 4. Our structures confirm expectations from mass spectrometry[11,12] that the C1, C2 and doublet microtubules have mostly distinct protein repertoires. The only proteins common to the singlet microtubules of the CA and the surrounding doublet microtubules are the calcium-binding protein, calmodulin, and FAP20. FAP20 links the A and B tubules of the doublet microtubule[2,20] but attaches to the C2 microtubule through an

entirely different mechanism that involves little contact with the tubulin surface (Extended Data Fig. 5a).

MIPs remodel tubulin and stabilize the lattice

In contrast to expectations from an electron cryotomography (cryo-ET) study of the *Chlamydomonas* CA[5], the luminal surfaces of both microtubules are bound by multiple microtubule inner proteins (MIPs; Fig. 2), although the number is far fewer than the 33 MIPs identified in *Chlamydomonas* doublet microtubules[2]. Many of these MIPs hug the contours of the microtubule lattice and lack globular domains, explaining why densities for only the two largest MIPs (FAP196 and FAP225) were observed previously by cryo-ET[5]. FAP196 is structurally similar to FAP52, a MIP of the doublet microtubule with twin β-propeller domains[2]. FAP52 functions in microtubule stabilization[21], suggesting that FAP196 may have similar role in stabilizing the C2 microtubule. However, the number of MIPs cannot be used as a proxy for microtubule stability, as the C2 microtubule is less stable than the C1 microtubule[14] despite having more MIPs.

We identify two major classes of non-globular MIP that are present on both microtubules: SAXO proteins and arc-MIPs. Arc-MIPs are a novel class of MIP that bind the interface between α/β tubulin heterodimers in a lateral arc across the luminal surface of multiple protofilaments (Fig. 2a,b). Arc-MIPs (for example FAP105 on the C1 microtubule and FAP239 on the C2 microtubule) are characterized by few secondary structure elements and repetitive binding to neighboring protofilaments. Different arc-MIPs can alternate every 8-nm on the same set of protofilaments, which in C2 is established by their specific interactions with the β-propeller domains of FAP196, which repeat every 16 nm (Fig. 2b).

SAXO proteins (short for "stabilizer of axonemal microtubules") have longitudinally arranged Mn motifs each featuring a short α-helix at the intradimer interface between α- and β-tubulin[22]. In the CA, SAXO proteins occur on protofilaments 3–5 of the C1 microtubule (Fig. 2a) and protofilaments 7 and 10–12 of the C2 microtubule (Fig. 2b). As Mn repeats are similar, and their densities may be averaged after applying 16- or 32-nm periodicity, we cannot identify the individual SAXO proteins from the cryo-EM density alone. To test the possibility that one or more of the densities could be FAP236, a predicted SAXO protein that is relatively abundant in our sample (together with FAP203 and FAP257)[2], we determined cryo-EM structures of both CA microtubules from a *fap236* mutant (Methods). Compared to the wild-type structures, a single SAXO density was absent from each microtubule (on protofilament 4 of C1 and protofilament 11 of C2) (Extended Data Fig. 6). We therefore assigned these densities to FAP236. This result also demonstrated that the CA contains multiple SAXO proteins, consistent with the different appearances of their densities (Fig. 2a,b). Our previous identification of SAXO proteins on *Chlamydomonas* doublet microtubules (FAP363)[2] and on the cortical microtubules of *Toxoplasma gondii* (SPM1)[22] suggests that SAXO proteins are common partners of architectural microtubules.

The CA MIPs not only bind the microtubule surface but actively remodel tubulin structure and lattice contacts. Similar to what has been observed for ciliary doublet microtubules[2], some MIPs stabilize the K40 loop of α-tubulin (residues 37–48) (Fig. 2c and Extended Data Fig. 7), which is typically invisible in cryo-EM structures of *in vitro* assembled microtubules

(Extended Data Fig. 7f) [23]. This is taken to the extreme in the C2 microtubule by the dramatic remodeling of the H1'-S2 loop (residues 47–64) of α-tubulin into an α-helix by FAP225 at the lateral interface between protofilaments 1 and 2 (Fig. 2d and Extended Data Fig. 7e). This remodeling allows FAP225 to substitute part of the H1'-S2 loop and form a contact-enhanced lateral interface. In addition, some MIPs insert into the taxol-binding pocket of β-tubulin (Fig. 2e), occupancy of which is known to stabilize microtubules[24]. Binding of MIPs to this pocket has been observed for ciliary doublet microtubules[2,25] but is again taken to the extreme in the C2 microtubule, with almost 90% of taxol-binding pockets occupied by MIPs.

In addition, each microtubule has at least one arc-MIP and exterior-bound protein that interacts with components on the opposing surface by protruding through the microtubule wall (Fig. 2f,g). This observation further implicates MIPs in coordinating the registers of the internal and external periodicities of microtubules[2,26]. Consistent with their seemingly important roles in CA assembly and stability, *Chlamydomonas* mutants of six MIPs we have examined showed slow swimming phenotype (Extended Data Fig. 6c and Supplementary Tables 2 and 3).

Establishing projection asymmetry

Although the C1 projections are morphologically distinct and bind different protofilaments of the microtubule surface, we discovered that most are built on foundations of a PF16 homodimer. PF16 is a conserved armadillo (ARM)-repeat protein that is required for the stable formation of the C1 microtubule in *Chlamydomonas*[27] and human sperm motility[28]. In our structure of the C1 microtubule, the PF16 homodimers bind alternating interprotofilament clefts to form discontinuous right-handed spirals that wrap around the left-handed microtubule, generating an imperfect three-start helix (Fig. 3a). Each spiral extends for 10 PF16 dimers and is capped by FAP194, a paralog of PF16 (Extended Data Fig. 8). The C-terminal ARM repeats of neighboring copies of PF16 interact above the microtubule surface, generating a cross-section resembling a six-petal flowerhead (Fig. 3b). Leucine-rich repeat kinase 2 (LRRK2), a protein with mutations associated with Parkinson's disease, also forms right-handed double helices on microtubules[29], suggesting that helical wrapping of proteins around microtubules may be a common theme in biology.

If each C1 projection has similar foundations provided by PF16, how are their unique identities generated? The answer lies partly in the ASH (ASPM, SPD-2, Hydin) domain, an all-β domain found in at least eight CA-associated proteins[30,31]. Our structures show that ASH domains occur in strings of consecutive domains (Fig. 3c), not unlike the repetitive immunoglobulin-like domains of extracellular receptors. Hydin, the largest of the ASH domain-containing proteins, has 33 ASH repeats based on AlphaFold predictions[32] (Extended Data Fig. 4), considerably more than previously identified[31]. The terminal ASH domain of these strings interacts with the interface between PF16 and the microtubule surface in a protofilament-specific manner, such that each of the five identified ASH-domain-containing proteins of the C1 microtubule (FAP47, FAP74, FAP81, FAP221 and Hydin) bind different protofilament/PF16 combinations (Figs. 3c,d and 4).

The importance of ASH proteins in establishing projection identity is seen in their phylogenetic conservation[31] and the selective loss of individual projections when they are absent or depleted. *Chlamydomonas fap81* mutants have no C1e and C1c projections[33] whereas *fap74* knockdown mutants have no C1d projections[34], observations consistent with the locations of FAP81 at the base of C1a/e/c and FAP74 at the base of C1d. Interestingly, RNAi knockdown of *Hydin* causes loss of the C2b projection[35] despite our unambiguous positioning of Hydin within the C1b projection. Given the neighboring positions of these two projections within the CA and the large size of Hydin (~0.5 MDa), it is likely that Hydin spans both projections and provides a tether between the C1 and C2 microtubules. The extraction of Hydin with the C1 microtubule may explain why the C2b projection is lost in our sample. Another large ASH protein, FAP47, binds on the C1-side of the bridge and like Hydin has been previously assigned to the C2 microtubule[11], suggesting it too may bind both microtubules. Consistent with these proteins spanning both microtubules, we observe weak density near the assigned models of Hydin and FAP47 at the C1-C2 bridge (Fig. 1b). These observations support a role for ASH proteins in tethering the CA microtubules to one another.

The presence of different PF16/ASH combinations at unique sites of the C1 microtubule raises the question of what directs ASH proteins to specific protofilaments? We analyzed each combination and found remarkable diversity in their interactions with the microtubule surface (Fig. 4). All have additional elements that recognize features of their vicinal microtubule environment or an interface that involves other microtubule-binding proteins. FAP74 and FAP81 use the first strategy; they both have extended N-termini that bind the microtubule surface. The binding of FAP47, FAP221, and Hydin all involve a third protein (FAP219, FAP108, and CPC1, respectively) that occupies the gap between the PF16 homodimer and the external interprotofilament cleft. Local microtubule curvature may also play a role in helping direct PF16/ASH combinations to specific protofilaments. Calculation of the interprotofilament angle for each pair of protofilaments in the C1 microtubule reveals more variation than occurs with *in-vitro* assembled and undecorated microtubules, which have near-uniform curvature except at the seam (Extended Data Fig. 9). The C2 microtubule also has irregular curvature but does not have the same distortion as the C1 microtubule (Extended Data Fig. 9). The variability in microtubule curvature could be induced by proteins binding to the interior or exterior of the microtubules. A role for MIPs in modulating the lateral angle between protofilaments has been proposed previously based on analysis of doublet microtubules[25].

The PF16/ASH combinations form a coordinate system on the tubulin lattice, with PF16 binding in the lateral direction and the ASH proteins binding in the longitudinal direction (Fig. 3c and Fig. 4) to recruit other proteins. A prime example is the recognition of PF16 and Hydin by FAP69 and CPC1 at the base of the C1b projection (Fig. 5b). These interactions are likely conserved in humans, as individuals with *HYDIN* mutations are deficient in the human CPC1 ortholog, SPEF2[17]. Most of the distal components of the C1b projection bind CPC1, so its correct recruitment and positioning is critical to the formation of the C1b projection[14], and ciliary motility in *Chlamydomonas*[14] and humans[17] (Supplementary Table 2).

Establishing projection periodicity

The PF16 spirals appear to be important determinants of the 16- and 32-nm periodicities of the C1 microtubule (Fig. 3e), in stark contrast to the linear coiled-coils that determine the 24- and 96-nm external periodicities of doublet microtubules[3,36]. As mentioned, the PF16 spirals are not continuous but interrupted by a cap of FAP194 that repeats every 32 nm (Fig. 3a and Extended Data Fig. 8). This disruption generates a 16-nm repeat for the regions of the C1 microtubule (C1a, C1b, and the C1-C2 bridge) that face the C2 microtubule, and 32-nm periodicity for the C1c-f projections (Fig. 3e) that matches the distance between radial spokes on the doublet microtubule[37]. Steric blocks from FAP46 and the ASH domains of FAP74 and FAP81 may help prevent the continuation of the PF16 spiral until it begins again on protofilaments 1/13. Other mechanisms, such as the recruitment of a single molecule of CPC1 to two adjacent C1b projections (Fig. 5b), likely helps to reinforce periodicity.

In contrast, the C2 microtubule lacks PF16 spirals and has 16-nm periodicity only. The internal 16-nm periodicity may be established by the twin β-propellers of FAP196 (Fig. 2b), which have a footprint greater than 8 nm, whereas the external 16-nm periodicity appears to be set by the domain structure of PF20 (Extended Data Fig. 4). PF20 has a C-terminal β-propeller domain that binds with 8-nm periodicity to the seam of the C2 microtubule and a coiled-coil domain that dimerizes with its neighboring copy, causing PF20 to transition from 8- to 16-nm periodicity (Fig. 3f). The coiled coil sits at the base of the C2a projection where it is likely required for its assembly (Fig. 5d). The PF20 β-propeller domain is directed to the seam of the C2 microtubule through its interaction with FAP178, a protein with a calponin homology (CH) domain that recognizes the heterotypic interactions between α-β tubulin that only occur at the seam (Extended Data Fig. 5b). The binding of PF20 at the seam of the C2 microtubule and the alignment of the seams of both microtubules at the bridge (Fig. 1b) lead us to propose a seam-centric model for the assembly of the CA. In this model, initial binding to the seam orients the C1 and C2 microtubules into their paired arrangement and establishes asymmetry, so that each projection is consistently attached to a specific protofilament. The importance of PF20 in this model explains why the entire CA is lost in *pf20* mutants[38].

Atomic models of the distal projections

Our structural information also reveals the domain-level organization of most of the CA projections. Guided by mass spectrometry data, fold recognition, structure predictions, and side-chain information (Methods and Extended Data Fig. 2), we built atomic models of all six projections of the C1 microtubule and the C2a and C2e projections of the C2 microtubule (Fig. 5 and Supplementary Table 1). The C1a, C1b and C2a projections are the largest and are morphologically similar to radial spokes, with which they interact. They have narrow microtubule-bound stalks and large distal heads, although the distal domains of the CA projections are less flat than radial spoke heads. There are also common themes in their protein repertoires, with the structures enriched in nucleotide-binding domains (see later), Membrane Occupation and Recognition Nexus (MORN) repeats, DPY30 motifs and calcium-binding domains[3] (Extended Data Fig. 4). The presence of calmodulin molecules bound to the IQ motifs of a long helix of MOT17 at the base of the C1a projection is

reminiscent of the FAP253/calmodulin interaction at the base of radial spoke 1 (Fig. 5a) and implicates calcium in regulating the conformation or dynamics of the C1a projection.

The structures also reveal how the distal regions of the projections interact with one another. The neighboring C1a and C1e projections are connected by a network of α-helices, suspended above the structure like a series of tightropes (Fig. 5a). These helices come from V-shaped heterodimers of two homologous proteins, FAP114 and FAP119, that are attached to both the C1a and C1e projections. The C-termini of three of the proteins (2 from C1a and 1 from C1e) come together to from a helical bundle midway between the projections, allowing the 16-nm periodicity of the C1a projection to connect to the 32-nm periodicity of the C1e projection (Fig. 5a). The interaction between the C1a and C2a projections likely involves PF6 in the C1a projection (Fig. 1b and 5a) and FAP147 in the C2a projection. Beneath PF6 is a highly unusual array of three-helical bundles formed by an algal-specific protein, FAP7, although whether this bundle is involved in the interface is unclear.

Interactions with radial spokes

The CA-spoke axis has been proposed to regulate axonemal dynein activity through both mechanical and chemical signals (reviewed in[39]). Mechanosignals are proposed to originate through distal-end interactions between radial spokes and the CA projections[40]. Cryo-EM structures of radial spokes and their spoke heads have recently revealed that their distal surfaces are highly negatively charged[3,41]. Neutralization of this charge disrupted *Chlamydomonas* swimming patterns[41], suggesting that electrostatics are important for the regulation of ciliary motility. We therefore analyzed the surface electrostatics of the distal surfaces of the C1a, C1b, and C1d projections that are most likely to interact with the negative-charged surfaces of radial spokes. We found that, unlike radial spokes, each of the projections had scattered regions of both positive and negative charge and no single charge dominated (Extended Data Fig. 10a). The projections do contain loops of both basic and acidic residues that are not resolved in our cryo-EM maps (Extended Data Fig. 10b), presumably due to flexibility. However, even if these loops were to be included in the electrostatic calculations, the overall pattern of discontinuous charge is likely to remain.

Chemical signals proposed to regulate ciliary motility include both nucleotides and phosphorylation. Although we identify two copies of the catalytic subunit of Protein phosphatase 1 (PP1c) (Extended Data Fig. 3b), neither copy is likely sufficiently exposed to have access to known phosphorylation sites within radial spokes[42]. A regulatory role for nucleotides in the CA-spoke axis was strengthened by the discovery of nucleotide-binding domains in the heads of radial spokes[3,41]. Here, we identified a cluster of two adenylate kinase domains (one each from FAP42 and CPC1) and five guanylate kinase domains from FAP42 in the C1b projection. Hydin, another C1b component, also has a predicted adenylate kinase domain[30], although this was not resolved in the structure. The resolved adenylate and guanylate kinase domains have the hallmarks of active enzymes and density consistent with bound nucleotides (Fig. 6), suggesting they are respectively capable of interconverting two ADP molecules into ATP and AMP, and consuming ATP to phosphorylate GMP. A homodimer of enolase, an enzyme that functions in the glycolytic pathway to produce ATP from 3-phosphoglycerate, is also observed in the same C1b projection (Fig. 6e)[43]. The

clustering of domains capable of consuming or producing ATP within a single projection of the C1 microtubule is likely functionally relevant. In *Chlamydomonas*, the CA is twisted around its longitudinal axis[5,44] and rotates by 360° between successive beats[45–47]. These two properties preferentially place the C1 projections at the outer bend[48] where the axonemal dyneins are active[49]. As axonemes consume ~230,000 molecules of ATP per beat cycle[50], they may be sensitive to local fluctuations in ATP/ADP ratio that could be exacerbated by the activity of domains with the C1b projection. Consistent with this model, loss of the C1b projection caused by mutations in *CPC1*, leads to a reduced flagella beat frequency[14] that can be restored by adding saturating levels of ATP[51]. PF6 in the C1a projection also has an adenylate kinase domain, which is positioned near the interface with the C2b. However, the density for this domain is poor, and we cannot conclude if it binds nucleotides or not.

Discussion

Microtubules are important cytoskeletal components that are given unique physical, chemical and signaling properties *in vivo* by microtubule-associating proteins. Understanding how microtubules, which have pseudohelical symmetry, become asymmetrically and periodically patterned *in vivo* by microtubule-associating proteins is important as the geometric organization of microtubule complexes, such as those found in the cilium and centriole, defines their function. Here, we have used cryo-EM to determine structures of the two extensively decorated microtubules of the ciliary central pair apparatus. Both microtubules have 13 protofilaments made up of identical copies of tubulin and yet have different periodic decorations and few proteins in common. In the two structures, we have identified and built atomic models of 48 different proteins that either directly interact with the microtubule surface or are components of the microtubule-bound projections. These structures, therefore, have massively expanded our understanding of the types of protein that can bind microtubules and the mechanisms they use. This included the discovery of arc-MIPs, a previously unobserved class of protein that bind laterally to the luminal surfaces of microtubules. Crucially, we also identified different mechanisms by which the asymmetry and periodicity of the C1 and C2 microtubules are established. For the C1 microtubule, spirals of PF16 bound to ASH-domain proteins combine to create a coordinate system that covers the microtubule to recruit other proteins with 16 or 32-nm periodicity. In contrast, the C2 microtubule lacks PF16 spirals but uses an adaptor protein, PF20, to convert the intrinsic 8-nm repeat of tubulin into 16 nm by forming dimers on the microtubule surface. The binding of PF20 at the seam of the C2 microtubule and the alignment of the seams of C1 and C2 microtubules (so that they face one another at the bridge) indicates a seam-centric model for the assembly of the CA.

Our structures of the CA microtubules are a step towards a complete atomic model of the axoneme. Further work will be required to fully resolve the C2b,c,d projections and the connecting bridge. These regions likely contain many of the proteins that have been identified as components of the CA by mass spectrometry but were not assigned in our structures (Extended Data Fig. 3c).

In conclusion, our structures have uncovered mechanisms by which microtubules become asymmetrically and periodically patterned and have provided the structural basis to elucidate the roles of individual CA proteins in the regulation of ciliary motility. Many of the identified proteins are conserved across species and are associated with human ciliopathies (Supplementary Table 2). Therefore, our work establishes a foundation for understanding human diseases such as MMAF and PCD.

Methods

No statistical methods were used to predetermine sample size. The experiments were not randomized, and investigators were not blinded to allocation during experiments and outcome assessment.

Analysis of *Chlamydomonas* MIP mutants

Strains of insertional mutants were obtained from the CLiP collection[56,57] at the Chlamydomonas Resource Center (University of Minnesota). The strains are: LMJ.RY0402.201666 (*fap236–666*); LMJ.RY0402.178940 (*fap105–940*); LMJ.RY0402.188283 (*fap105–283*); LMJ.RY0402.096435 (*fap275–435*); LMJ.RY0402.251824 (*fap275–824*); LMJ.RY0402.127348 (*fap196–348*); LMJ.RY0402.172992 (*fap213–992*); LMJ.RY0402.199434 (*fap239–434*) and LMJ.RY0402.162848 (*fap424–848*). Each strain was crossed by CC-4402 (wild type) to remove the cell wall-less mutant and a phototactic mutant that are present in the parental strain (CC-4533) used for the CLiP collection. Meiotic progeny showed slow swimming as judged by light microscopy (Extended Data Fig. 6c and Supplementary Table 3), resistance to paromomycin, and lack of a PCR fragment using primers (provided in Supplementary Table 4) around the insertion.

Swimming velocity was measured using bright field microscopy as previously described[58]. For each recording, 10 μL cells were pipetted onto a slide and covered with an 18 × 18 mm coverslip, which generated a fluid layer about 30 μm thick. The slides were imaged using a Zeiss AxioPhot with a 100x Neofluar oil-immersion objective lens (Carl Zeiss AG) in a climate-controlled room at 21°C. Microscope settings were adjusted to provide the greatest contrast between the cilium and background. Videos were captured at 320 × 240 resolution and 2,000 frames per second (fps) using a Phantom Miro eX2 camera and Phantom Camera Control Application 2.6 (Vision Research). Approximately 1,000 frames (spanning 0.5 s) were extracted and saved as uncompressed AVI (Audio Video Interleaved) files at 15 fps. Swimming velocities were measured from the videos using MATLAB R2016a (MathWorks).

For the *fap236* mutant, drug resistance and the lack of the PCR fragment co-segregated in 34 tetrads after two backcrosses to strain CC-4402. We examined mRNA from three wild-type strains and three verified *fap236* mutant strains using three sets of primers that cross exon boundaries. The cDNA from *fap236* was amplified with primers in exon 1 and 2, but not with primers in exons 2 and 3 or primers in exons 3 and 4. In contrast, PCR products were obtained from wild-type cDNA for all three sets of primers.

RNA was isolated from flagellated *Chlamydomonas* cells. To induce flagellation, cells grown for 5 days on two R medium agar plates were transferred to 40 ml nitrogen-free medium (M-N/5) and left for 2 h at room temperature. RNA was extracted from the cells with the RNeasy Mini Kit (Qiagen) following the manufacturer's instructions. The RNA (2 μg) was reverse transcribed using SuperScript III (Invitrogen) according to the manufacturer's recommendation and with random primers as described[59].

Sample preparation

Axonemes were isolated from wild type and *fap236* mutant *Chlamydomonas* cells and dissociated into microtubules as previously described[2]. Briefly, cells in HMDS buffer (10 mM HEPES, 5 mM $MgSO_4$, 1 mM DTT, 4% Sucrose, pH 7.4) were treated with 25 mM dibucaine (Sigma-Aldrich) to induce deflagellation. Cell bodies were removed by centrifugation at 1,800 x *g* for 5 min. The flagella-containing supernatant was collected and laid over a 25% sucrose suspension in HMDS buffer. After centrifugation at 2,400 x *g* for 10 min, the supernatant was collected down to the sucrose interface. NP-40 (USB Chemicals) was added to the flagella to a final concentration of 1% to remove membranes. Axonemes were collected by centrifugation at 30,000 x *g* for 20 min and then resuspended in HMDEKP buffer (30 mM HEPES, 5 mM $MgSO_4$, 1 mM DTT, 0.5 mM EGTA, 25 mM KCl, pH 7.4) containing 1x ProteaseArrest protease inhibitors (G-Biosciences). The volume and optical density (at 280 nm) of the purified axonemes was adjusted to 10 μL and 32 absorbance units. Then the sample was mildly digested in HMDEKP buffer containing 10 μg/mL subtilisin A (Sigma-Aldrich) and 2 mM ATP, in the presence of ProteaseArrest protease inhibitors. Protease digestion was performed on ice and stopped after 30 min by plunge freezing.

Cryo-EM data processing

Cryo-EM data were collected across multiple sessions using the Titan Krios microscopes at either Washington University in St. Louis (WUSTL) or Case Western Reserve University (CWRU). The data collection parameters are listed in Table 1. Some of the data were reported previously and used to determine the structure of the *Chlamydomonas* doublet microtubule[2]. A total of 9,271 movies for the wild type and 4,099 movies for the *fap236* mutant containing CA microtubules were drift-corrected and electron-dose weighted using *patch motion correction* in cryoSPARC[60]. The contrast transfer function (CTF) parameters for different regions within a drift-corrected micrograph were estimated using *patch CTF estimation* in cryoSPARC. To process microtubule data using single-particle methods[61], C1 and C2 microtubules were manually selected from the drift-corrected micrographs using the APPION image-processing suite[62]. Interestingly, almost all the C2 microtubules are within loosely associated pairs, whereas the C1 microtubules also appear on their own (Extended Data Fig. 1a,b). This observation is consistent with prior reports that C2 microtubules are less stable than C1 microtubules[14].

The selected microtubule segments were computationally cut into overlapping boxes (512×512 pixels) with 16-nm step between adjacent boxes. We refer to these boxed images as 16-nm particles. The choice of 16-nm step size was based on prior knowledge of C1 and C2 microtubule periodicities from cryo-ET studies[5].

The microtubule particles from the different datasets (Table 1) were extracted from the drift-corrected micrographs in cryoSPARC and resampled to the same box size (512 pixels) and pixel size (1.39 Å) using *relion_image_handler* in RELION-3[63]. The exact scaling factor for each dataset was obtained by comparing their respective 3D reconstructions in Chimera[64]. The resampled particles were imported back to cryoSPARC and merged for further data processing. Merging datasets improved the final resolution in all cases.

The initial reference models of the C1 and C2 microtubules were created using the cryo-ET structure of the CA (EMD-9385)[5] with the microtubule part of the density replaced by a single-particle structure (EMD-7974)[23] filtered to 12 Å resolution. Next, we performed multi-reference sorting of all 16-nm particles using EMAN1[65], which also provides global alignment parameters for each particle. After successfully separating the dataset into two groups corresponding to C1 (~60 %) and C2 (~40 %) microtubules, we refined each group separately using FREALIGN v9.11[66]. Only local search of alignment parameters was used in this step. Once structures of the C1 and C2 microtubules with 16-nm periodicity were obtained by FREALIGN, we realigned all the microtubule particles using EMAN1 (for global search and classification) and FREALIGN (for local refinement). The particle sets with their alignment parameters were then imported to RELION-3 for another round of refinement followed by tubulin signal subtraction. A microtubule reconstruction from the same particle dataset was used for signal subtraction, using a tight soft-edged mask covering only the tubulin part in the reconstruction. In the next step, we performed 3D classification of the signal-subtracted particles of C1 microtubule in RELION-3 to separate the 16-nm particles into 32-nm particles using a soft-edged shape mask covering the C1f projection. We also did 3D classification of the signal-subtracted C2 microtubule particles to select the subset with PF20 bound at the microtubule seam or with C2c/d projections.

To improve local resolution, we used a divide-and-conquer strategy[2] by performing focused refinement in cryoSPARC for different regions. For the C1 microtubule, we divided the structure into six major sub-regions: the microtubule core, the outer shell, the C1a projection, the C1e/c projection, the C1f projection, and the C1b projection. Each sub-region was further divided into smaller pieces using various soft-edged shape masks (Extended Data Fig. 1c–f). For the microtubule core, assuming 16-nm periodicity, we divided it into seven pieces using wedge masks (160 Å in radius and 200 Å in length) each covering two protofilaments (Extended Data Fig. 1c). To compute the regions of the C1 microtubule with 32-nm periodicity, we performed focused refinement of a duplicate set of particles whose image center coordinates were shifted by 16-nm along the microtubule axis (using *Particle Extraction* in RELION-3). These center-shifted reconstructions were combined with the original reconstructions to produce the C1 microtubule map with 32-nm periodicity. The radial extensions (between radii 140 Å and 240 Å) of these wedge masks (which we call "shell" masks) were used to improve the local densities of the outer shell (with 32-nm periodicity) (Extended Data Fig. 1d). For the C2 microtubule with 16-nm periodicity, we divided the structure into two major sub-regions: the microtubule core and the C2a projection. The microtubule core was further divided into seven pieces using wedge masks (160 Å in radius and 200 Å in length) (Extended Data Fig. 1e). The large C1a, C1b and C2a projections were further divided into several pieces corresponding to the basal, intermediate, and distal parts (Extended Data Fig. 1f). We also performed focused

refinement using various shape masks covering different structural pieces within the outer shell, which typically produced better local resolution than using the shell masks. Since the reconstruction box size (512 pixels) was not large enough to fit all the densities of the projection, we shifted the center coordinates of the extracted raw particles (using *Particle Extraction* in RELION-3) so that the center of the reconstruction box is at the center of mass of each projection, then continued the focused refinement. Focused 3D classification and local refinement were also used to recover partial densities for the C2c/d projection and the bridge between microtubules (Fig. 1b).

Composite maps

To generate a composite map for model building and refinement, the 3D reconstructions from focused refinement in cryoSPARC were auto-sharpened using deepEMhancer[67]. All sharpened maps were multiplied by the modified version of their respective shape masks that have minimal overlaps between neighboring ones, and then aligned to a consensus map of either the C1 or C2 microtubule using the *fit in map* command in Chimera[64]. Finally, all the masked and aligned maps were resampled onto the same grid box and merged (using the *vop resample* and *vop maximum* command in Chimera) to produce a composite map. A larger grid box size (640 pixels) was needed to accommodate the whole structure of the C1 microtubule. The central portion of the composite map was extended to fill the entire box based on the 32-nm periodicity for better visualization and model refinement.

Model Building and Protein Identification

All model building was performed in Coot v.0.9.4.1 or v.0.9.5[68]. Model building was initiated by placing protofilaments from PDB 6U42[2] into the map density of the microtubules. Each chain of tubulin was then fit to the map using rigid-body refinement.

Protein identification was greatly facilitated by mass-spectrometry analysis of CA mutants[11,12]. Using the results of these studies, we built two sequence libraries of all the identified proteins of the C1 and C2 microtubules. As sequences can vary between databases, we included entries from Phytozome, UniProt and NCBI. Proteins in our cryo-EM maps were identified using these sequence libraries. Identification involved one of three strategies (Extended Data Fig. 2a). In the first strategy, a polyalanine model was manually built into the density using Coot and sidechains assigned based on visual inspection of the density. The derived sequence was then extracted from the model and used to query our custom sequence libraries using protein BLAST[69]. The model was then updated to match the sequence of the best solution. If no reasonable hit was obtained, the sequence was used to query the entire *Chlamydomonas* proteome available from the NCBI. In the second strategy, map subvolumes were extracted in Coot or Chimera and submitted to DeepTracer, a deep-learning-based method for automated model building[70]. The sequence was extracted from the built model and used to query both our bespoke sequence libraries and the complete *Chlamydomonas* proteome. An example of this method is shown in Extended Data Fig. 2b. The third strategy was to recognize globular protein folds in map subvolumes using the BALBES-MOLREP pipeline[71]. In addition to the BALBES library, we created a bespoke library of predicted protein models using SWISS-MODEL[72], i-TASSER[73] or Robetta[74]. During the latter stages of our model-building process, AlphaFold2 became

publicly available[32]. We then generated AlphaFold2 models for all the proteins in our sequence libraries and updated the rigid-body fitted homology models with AlphaFold2 models which enabled us to build more fragments and identify more proteins. PF6, FAP114, FAP119 and FAP227 were identified exclusively using AlphaFold2. A web-based implementation of AlphaFold2, ColabFold[75], was used to predict structures of proteins complexes and to check our modeled protein-protein interactions.

Refinement

The atomic models were subjected to iterative rounds of real-space refinement in Coot[68] and Phenix[76]. During real-space refinement in Coot, torsion, planar peptide, *trans* peptide, and Ramachandran restraints were used throughout with α-helical restraints applied when refining α-helices. The refinement weight for each map was estimated automatically and manually adjusted to give the best compromise between geometry and fit to density. During real-space refinement in Phenix, secondary structure and Ramachandran restraints were used, and the resolution limit was set to 3.8 Å. Each round of refinement was punctuated by model correction in Coot. Model validation was performed using MolProbity[77] integrated into Phenix. Model statistics are reported in Table 1.

Interprotofilament rotation angle measurement

To measure the interprotofilament angle, we used the 'angle_between_domains' command from PyMOL[78], as previously used to measure the interprotofilament angle in doublet microtubules[79]. This tool measures the relative rotation (in conjugation with necessary translation) from one α,β-tubulin dimer to the neighboring tubulin dimer in the lateral direction.
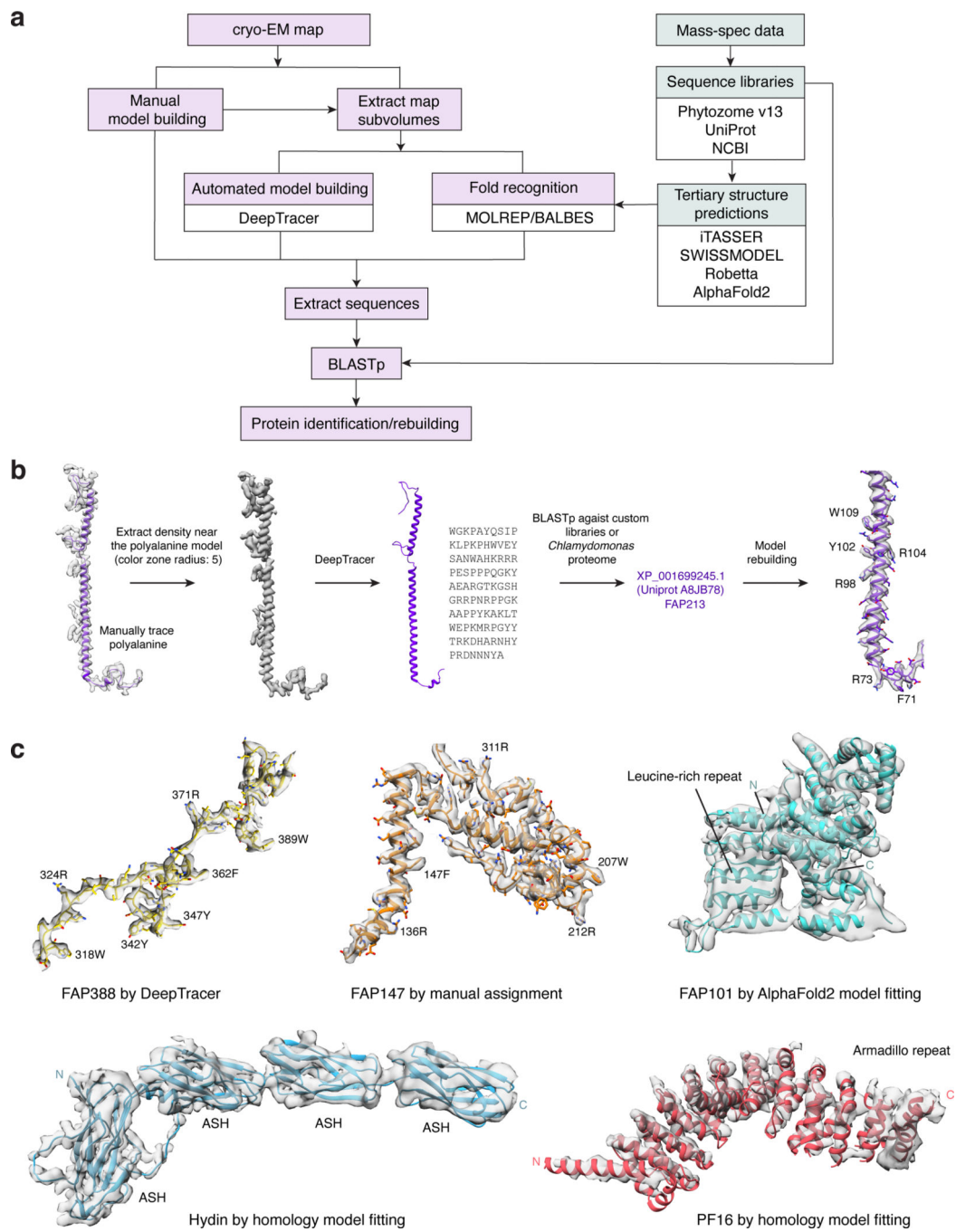
Figures

Figure panels were generated using Chimera[64], ChimeraX[80] or PyMOL[78].

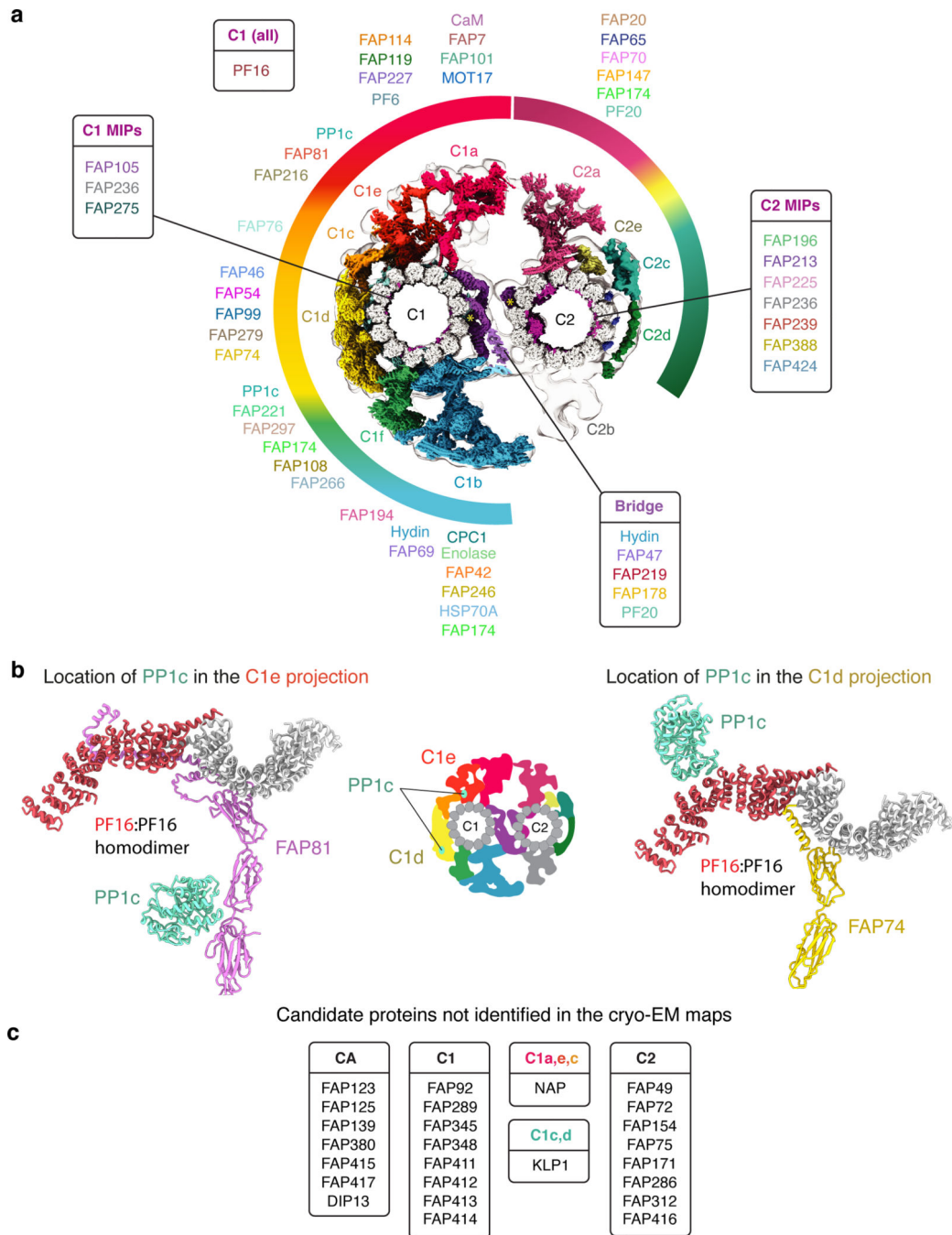Software used in the Brown laboratory were installed and configured by SBGrid[81].

Extended Data
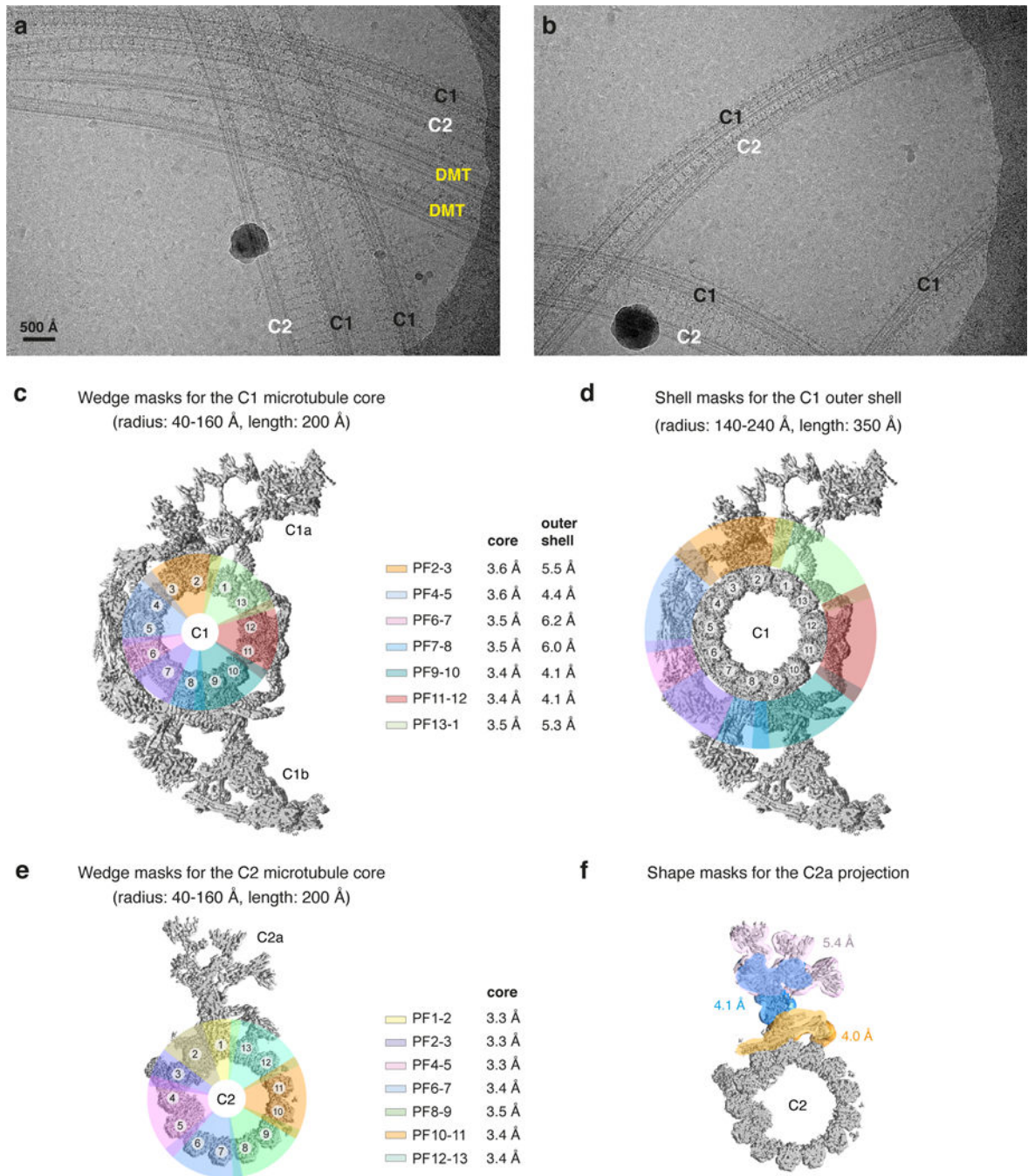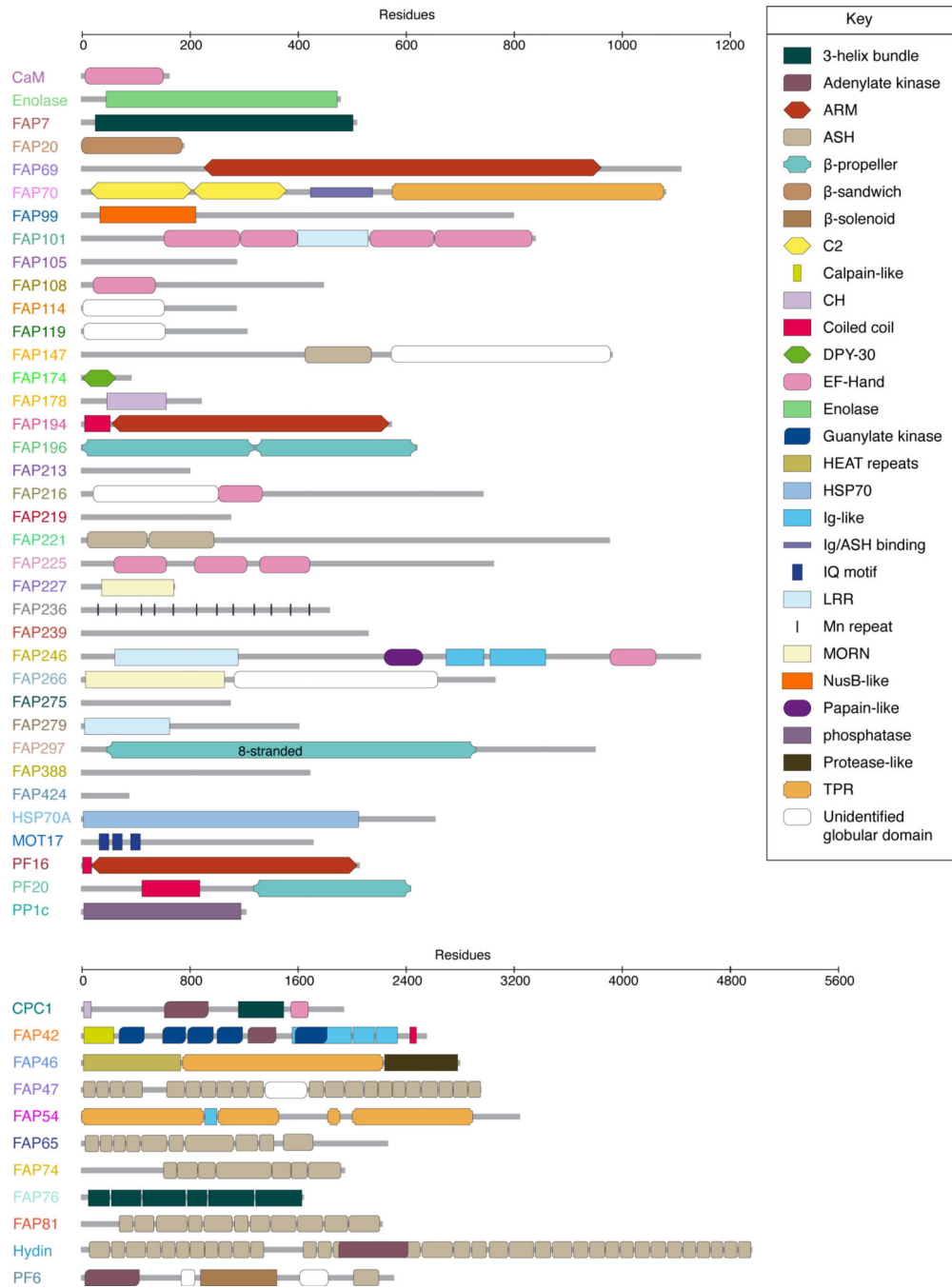

Extended Data Fig. 1 |.
Data processing.

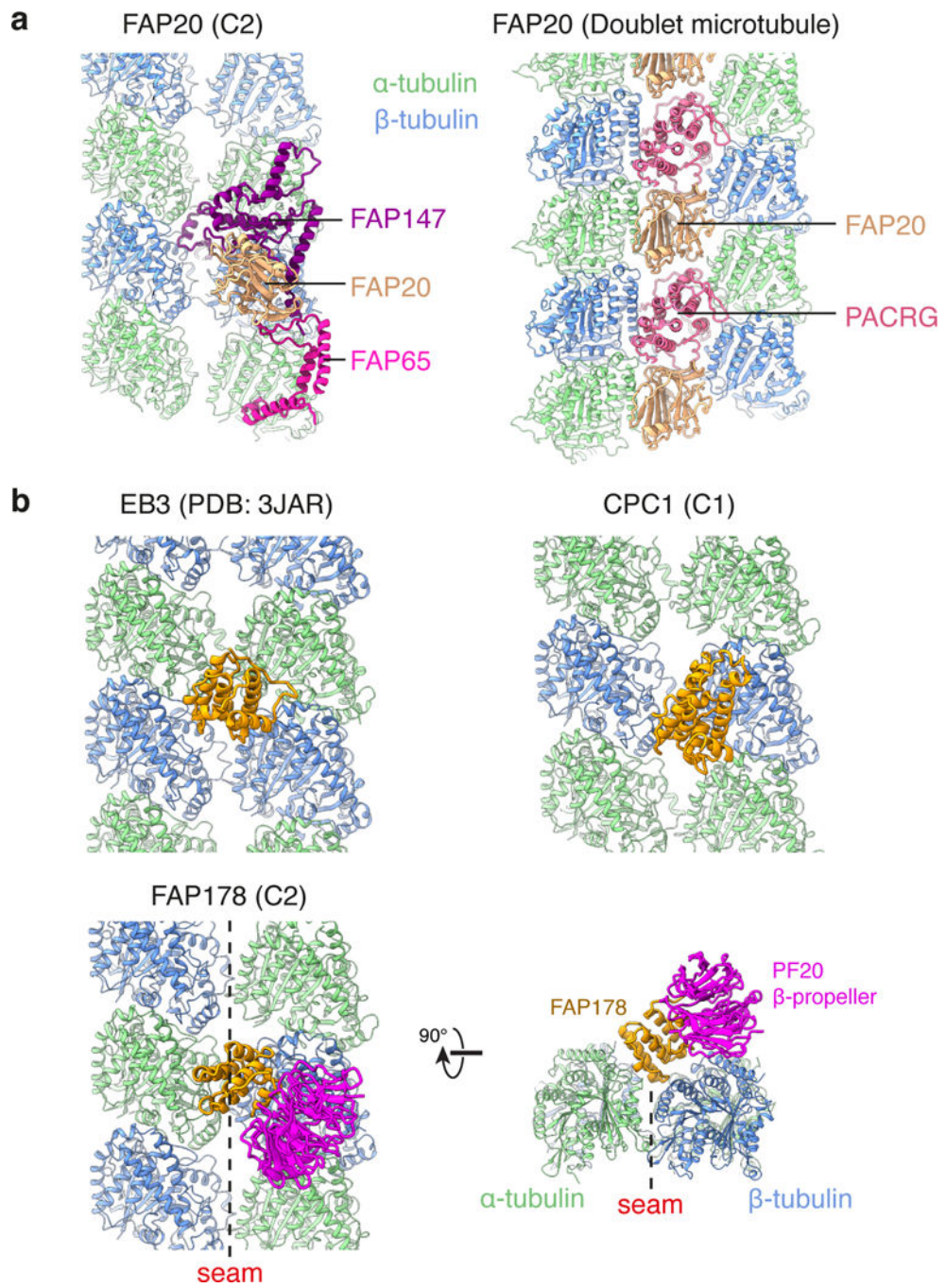**Extended Data Fig. 2 |.**
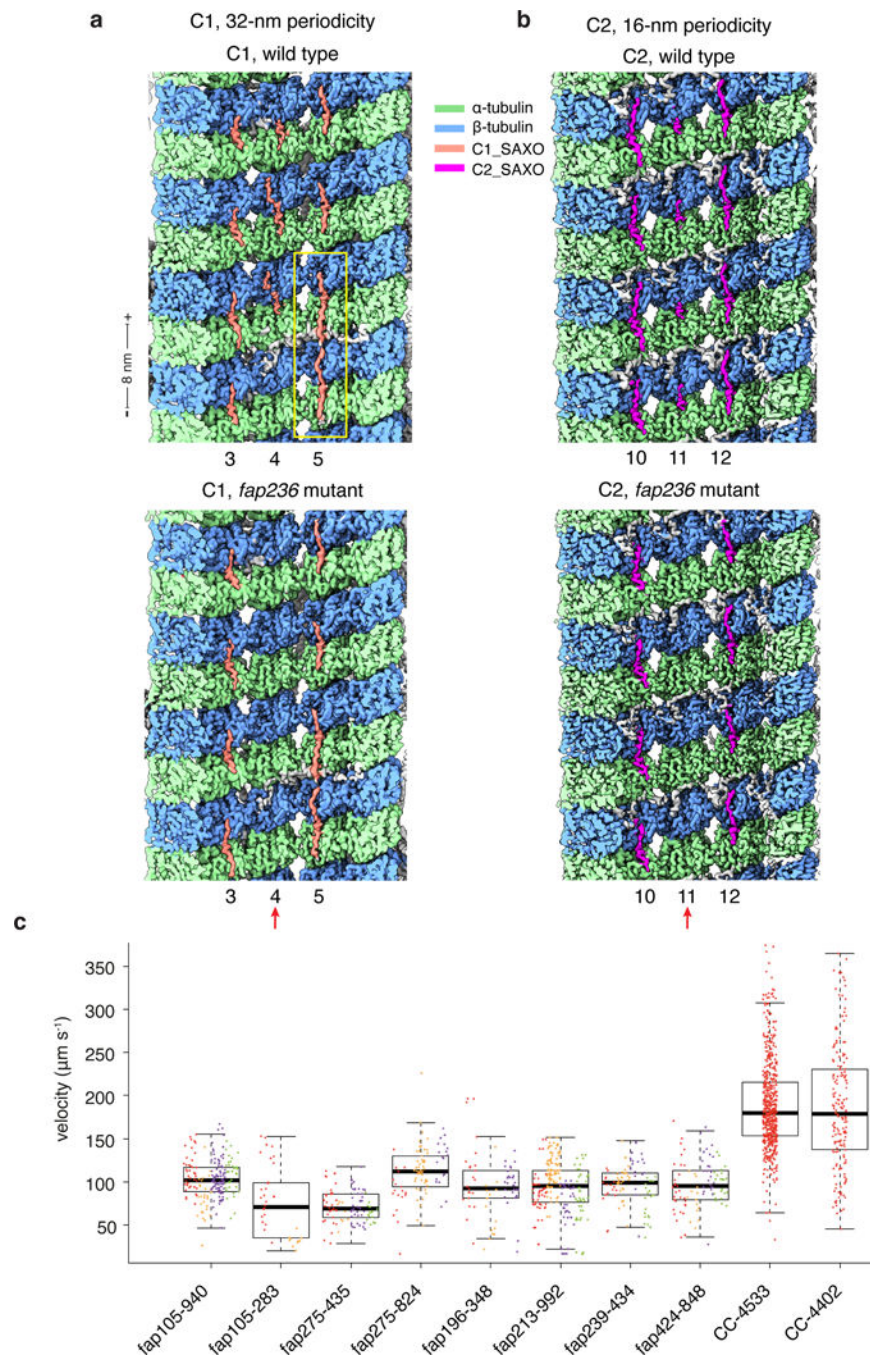Protein identification strategies.

Extended Data Fig. 3 |.
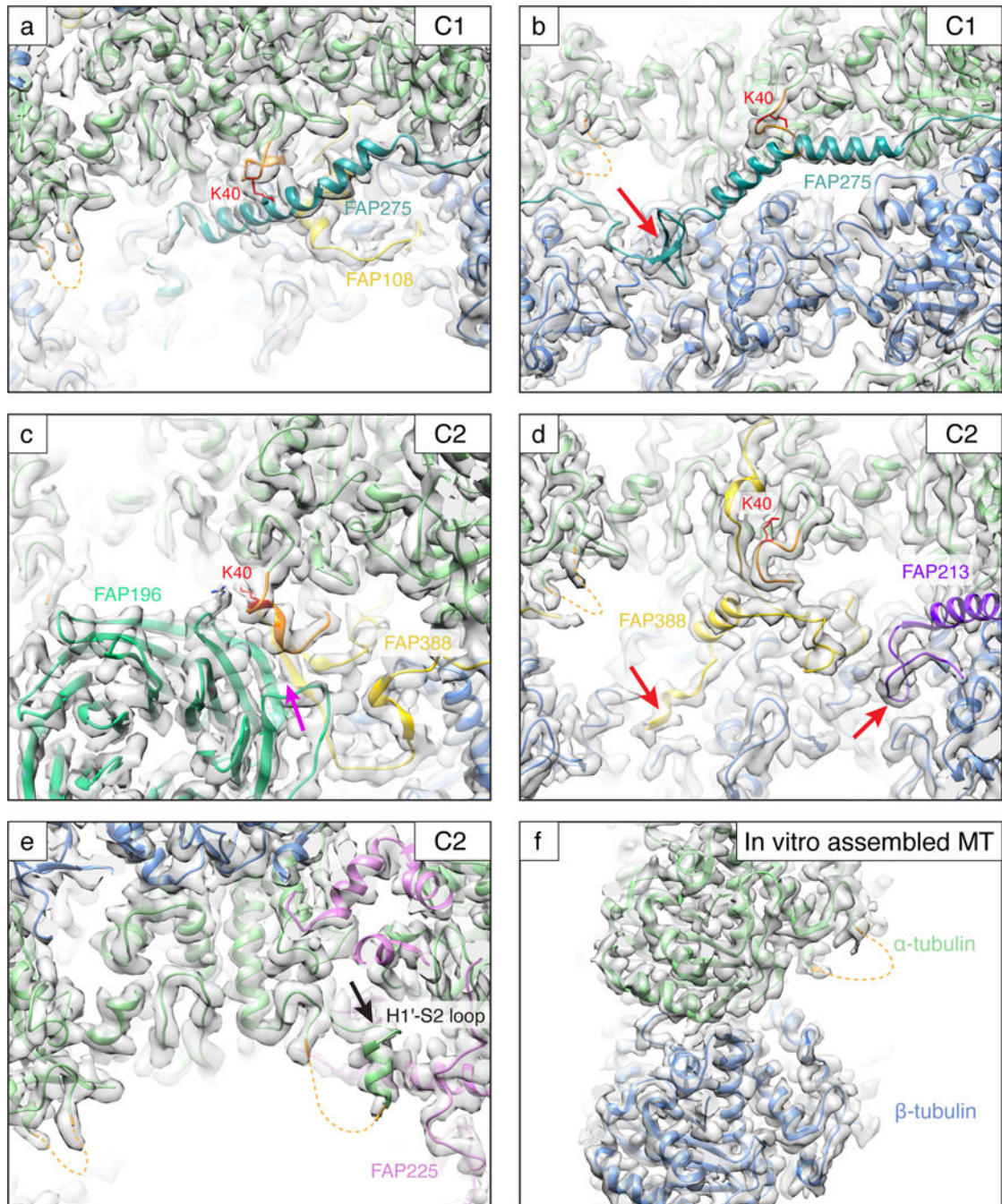Locations of proteins within the central apparatus (CA).

Extended Data Fig. 4 |.
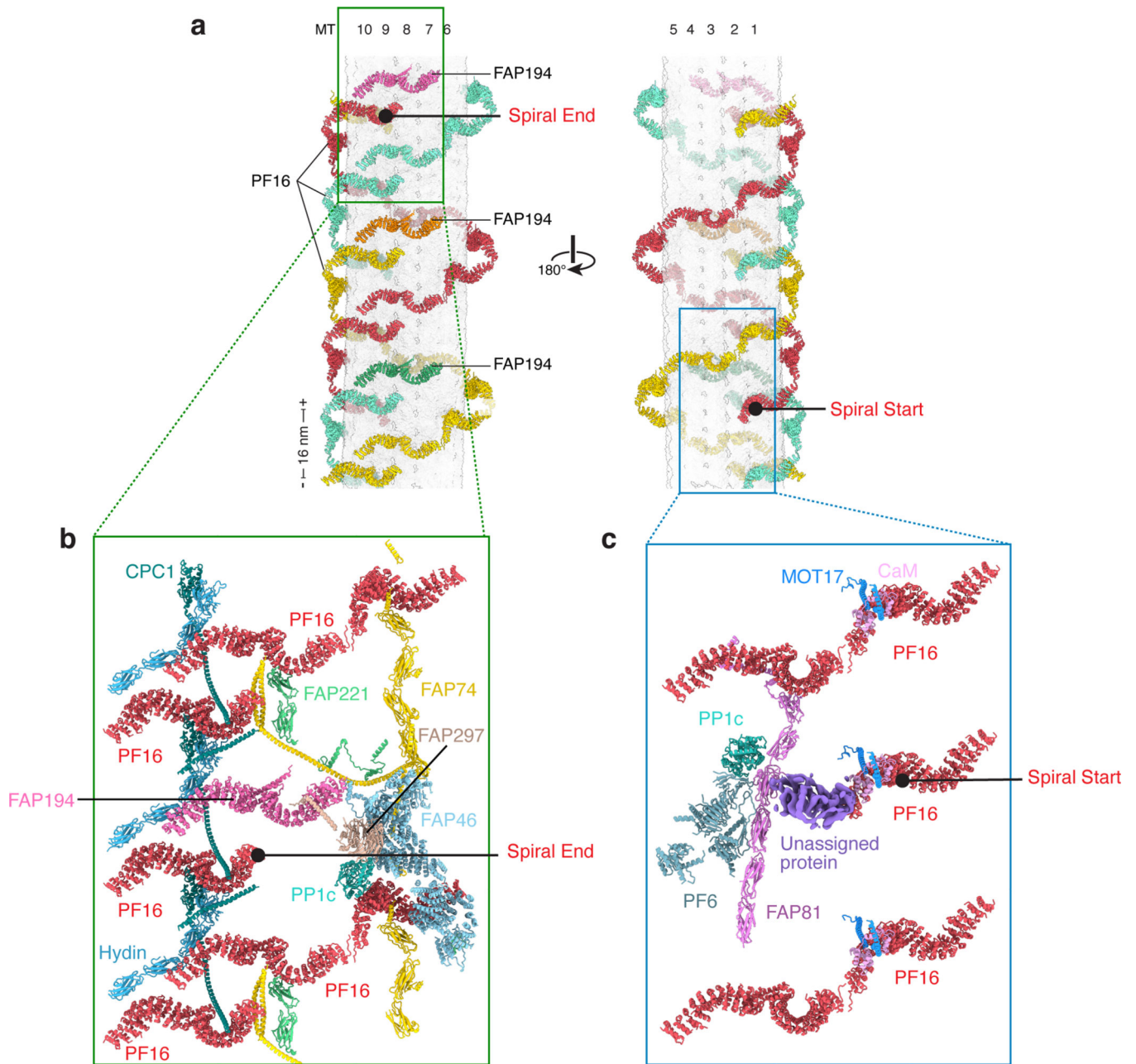Domain organization of central apparatus (CA) proteins.

Extended Data Fig. 5 |.
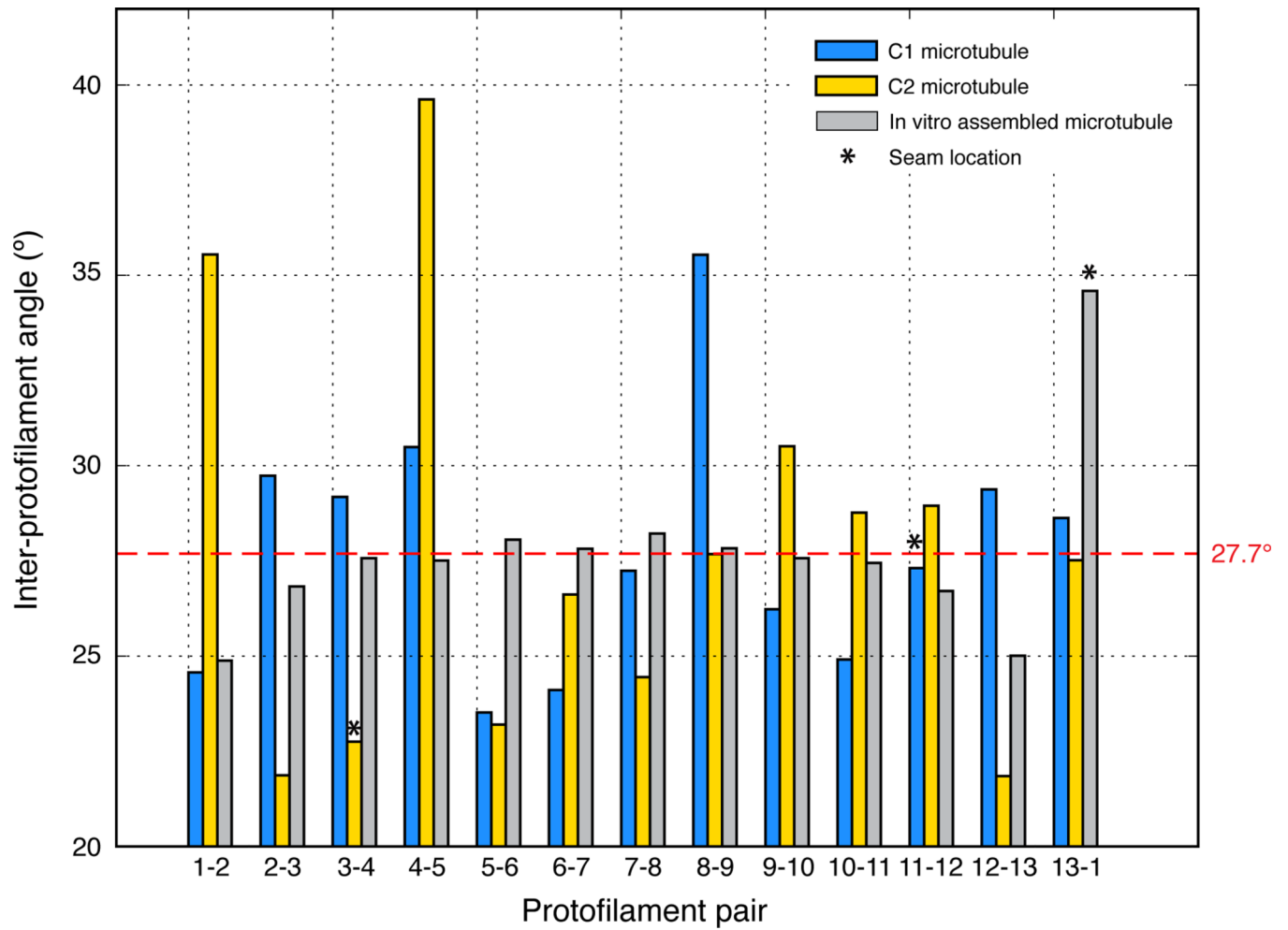Protein-microtubule interactions.

Extended Data Fig. 6 |.

Structural and functional analyses of Chlamydomonas mutants.

Extended Data Fig. 7 |.
Interactions between the K40 loop of α-tubulin and microtubule inner proteins (MIPs).

Extended Data Fig. 8 |.
Details of the PF16 spiral.

Extended Data Fig. 9 |.
Analysis of microtubule curvature.

Extended Data Fig. 10 |.
Projection surfaces colored by electrostatic potential.

Supplementary Material

Refer to Web version on PubMed Central for supplementary material.

Acknowledgments

Data Availability

The composite cryo-EM maps of the C1 and C2 microtubules are deposited in the Electron Microscopy Data Bank (EMDB; https://www.ebi.ac.uk/pdbe/emdb/) with accession codes EMD-25381 and EMD-25361. The original unsharpened maps from cryoSPARC are

associated with these depositions as additional files. The atomic models for the C1 and C2 microtubules are deposited in the Protein Data Bank (PDB; https://www.rcsb.org/) with accession codes 7SQC and 7SOM.

References

1. Mitchell DR Reconstruction of the projection periodicity and surface architecture of the flagellar central pair complex. Cell Motil. Cytoskeleton 55, 188–199 (2003). [PubMed: 12789663]

2. Ma M. et al. Structure of the Decorated Ciliary Doublet Microtubule. Cell 179, 909–922.e12 (2019). [PubMed: 31668805]

3. Gui M. et al. Structures of radial spokes and associated complexes important for ciliary motility. Nat. Struct. Mol. Biol 28, 29–37 (2021). [PubMed: 33318703]

4. Walton T, Wu H. & Brown A. Structure of a microtubule-bound axonemal dynein. Nat Commun 12, 477–9 (2021). [PubMed: 33473120]

5. Carbajal González BI et al. Conserved structural motifs in the central pair complex of eukaryotic flagella. Cytoskeleton (Hoboken) 70, 101–120 (2013). [PubMed: 23281266]

6. Leung MR et al. The multi-scale architecture of mammalian sperm flagella and implications for ciliary motility. EMBO J. 40, e107410 (2021).

7. Samsel Z, Sekretarska J, Osinka A, Wloga D. & Joachimiak E. Central Apparatus, the Molecular Kickstarter of Ciliary and Flagellar Nanomachines. Int J Mol Sci 22, 3013 (2021). [PubMed: 33809498]

8. Adams GM, Huang B, Piperno G. & Luck DJ Central-pair microtubular complex of Chlamydomonas flagella: polypeptide composition as revealed by analysis of mutants. J. Cell Biol 91, 69–76 (1981). [PubMed: 7028763]

9. Dutcher SK, Huang B. & Luck DJ Genetic dissection of the central pair microtubules of the flagella of Chlamydomonas reinhardtii. J. Cell Biol 98, 229–236 (1984). [PubMed: 6707088]

10. Wargo MJ, Dymek EE & Smith EF Calmodulin and PF6 are components of a complex that localizes to the C1 microtubule of the flagellar central apparatus. J. Cell. Sci 118, 4655–4665 (2005). [PubMed: 16188941]

11. Zhao L, Hou Y, Picariello T, Craige B. & Witman GB Proteome of the central apparatus of a ciliary axoneme. J. Cell Biol 218, 2051–2070 (2019). [PubMed: 31092556]

12. Dai D, Ichikawa M, Peri K, Rebinsky R. & Huy Bui K. Identification and mapping of central pair proteins by proteomic analysis. Biophys Physicobiol 17, 71–85 (2020). [PubMed: 33178545]

13. Warr JR, McVittie A, Randall J. & Hopkins JM Genetic control of flagellar structure in Chlamydomonas reinhardii. Genetics Research 7, 335–351 (1966).

14. Mitchell DR & Sale WS Characterization of a Chlamydomonas insertional mutant that disrupts flagellar central pair microtubule-associated structures. J. Cell Biol 144, 293–304 (1999). [PubMed: 9922455]

15. Bustamante-Marin XM et al. Identification of genetic variants in CFAP221 as a cause of primary ciliary dyskinesia. Journal of human genetics 65, 175–180 (2020). [PubMed: 31636325]

16. Olbrich H. et al. Recessive HYDIN mutations cause primary ciliary dyskinesia without randomization of left-right body asymmetry. Am. J. Hum. Genet 91, 672–684 (2012). [PubMed: 23022101]

17. Cindrić S. et al. SPEF2- and HYDIN-Mutant Cilia Lack the Central Pair-associated Protein SPEF2, Aiding Primary Ciliary Dyskinesia Diagnostics. Am J Respir Cell Mol Biol 62, 382–396 (2020). [PubMed: 31545650]

18. Liu C. et al. Deleterious variants in X-linked CFAP47 induce asthenoteratozoospermia and primary male infertility. Am. J. Hum. Genet 108, 309–323 (2021). [PubMed: 33472045]

19. Dong FN et al. Absence of CFAP69 Causes Male Infertility due to Multiple Morphological Abnormalities of the Flagella in Human and Mouse. Am. J. Hum. Genet 102, 636–648 (2018). [PubMed: 29606301]

20. Yanagisawa H-A et al. FAP20 is an inner junction protein of doublet microtubules essential for both the planar asymmetrical waveform and stability of flagella in Chlamydomonas. Mol. Biol. Cell 25, 1472–1483 (2014). [PubMed: 24574454]

21. Owa M. et al. Inner lumen proteins stabilize doublet microtubules in cilia and flagella. Nat Commun 10, 1143 (2019). [PubMed: 30850601]

22. Wang X. et al. Cryo-EM structure of cortical microtubules from human parasite Toxoplasma gondii identifies their microtubule inner proteins. Nat Commun 12, 3065–14 (2021). [PubMed: 34031406]

23. Zhang R, LaFrance B. & Nogales E. Separating the effects of nucleotide and EB binding on microtubule structure. Proc. Natl. Acad. Sci. U.S.A 115, E6191–E6200 (2018). [PubMed: 29915050]

24. Buey RM et al. Microtubule interactions with chemically diverse stabilizing agents: thermodynamics of binding to the paclitaxel site predicts cytotoxicity. Chem. Biol 12, 1269–1279 (2005). [PubMed: 16356844]

25. Ichikawa M. et al. Tubulin lattice in cilia is in a stressed form regulated by microtubule inner proteins. Proc. Natl. Acad. Sci. U.S.A 116, 19930–19938 (2019). [PubMed: 31527277]

26. Gui M. et al. De novo identification of mammalian ciliary motility proteins using cryo-EM. Cell 184, 5791–5806.e19 (2021). [PubMed: 34715025]

27. Smith EF & Lefebvre PA PF16 encodes a protein with armadillo repeats and localizes to a single microtubule of the central apparatus in Chlamydomonas flagella. J. Cell Biol 132, 359–370 (1996). [PubMed: 8636214]

28. Wu H. et al. Patients with severe asthenoteratospermia carrying SPAG6 or RSPH3 mutations have a positive pregnancy outcome following intracytoplasmic sperm injection. J. Assist. Reprod. Genet 37, 829–840 (2020). [PubMed: 32124190]

29. Watanabe R. et al. The In Situ Structure of Parkinson's Disease-Linked LRRK2. Cell 182, 1508–1518.e16 (2020). [PubMed: 32783917]

30. Ponting CP A novel domain suggests a ciliary function for ASPM, a brain size determining gene. Bioinformatics 22, 1031–1035 (2006). [PubMed: 16443634]

31. Zhao L, Hou Y, McNeill NA & Witman GB The unity and diversity of the ciliary central apparatus. Philos. Trans. R. Soc. Lond., B, Biol. Sci 375, 20190164 (2020). [PubMed: 31884923]

32. Jumper J. et al. Highly accurate protein structure prediction with AlphaFold. Nature 596, 583–589 (2021). [PubMed: 34265844]

33. Fu G. et al. Structural organization of the C1a-e-c supercomplex within the ciliary central apparatus. J. Cell Biol 113, jcb.201906006 (2019).

34. Brown JM, Dipetrillo CG, Smith EF & Witman GB A FAP46 mutant provides new insights into the function and assembly of the C1d complex of the ciliary central apparatus. J. Cell. Sci 125, 3904–3913 (2012). [PubMed: 22573824]

35. Lechtreck K-F & Witman GB Chlamydomonas reinhardtii hydin is a central pair protein required for flagellar motility. J. Cell Biol 176, 473–482 (2007). [PubMed: 17296796]

36. Oda T, Yanagisawa H, Kamiya R. & Kikkawa M. Cilia and flagella. A molecular ruler determines the repeat length in eukaryotic cilia and flagella. Science 346, 857–860 (2014). [PubMed: 25395538]

37. Barber CF, Heuser T, Carbajal González BI, Botchkarev VV & Nicastro D. Three-dimensional structure of the radial spokes reveals heterogeneity and interactions with dyneins in Chlamydomonas flagella. Mol. Biol. Cell 23, 111–120 (2012). [PubMed: 22072792]

38. Smith EF & Lefebvre PA PF20 gene product contains WD repeats and localizes to the intermicrotubule bridges in Chlamydomonas flagella. Mol. Biol. Cell 8, 455–467 (2017).

39. Smith EF & Yang P. The radial spokes and central apparatus: mechano-chemical transducers that regulate flagellar motility. Cell Motil. Cytoskeleton 57, 8–17 (2004). [PubMed: 14648553]

40. Oda T, Yanagisawa H, Yagi T. & Kikkawa M. Mechanosignaling between central apparatus and radial spokes controls axonemal dynein activity. J. Cell Biol 204, 807–819 (2014). [PubMed: 24590175]

41. Grossman-Haham I. et al. Structure of the radial spoke head and insights into its role in mechanoregulation of ciliary beating. Nat. Struct. Mol. Biol 64, 1073–9 (2020).

42. Wang H. et al. The global phosphoproteome of Chlamydomonas reinhardtii reveals complex organellar phosphorylation in the flagella and thylakoid membrane. Mol. Cell Proteomics 13, 2337–2353 (2014). [PubMed: 24917610]

43. Mitchell BF, Pedersen LB, Feely M, Rosenbaum JL & Mitchell DR ATP production in Chlamydomonas reinhardtii flagella by glycolytic enzymes. Mol. Biol. Cell 16, 4509–4518 (2005). [PubMed: 16030251]

44. Goodenough UW & Heuser JE Substructure of inner dynein arms, radial spokes, and the central pair/projection complex of cilia and flagella. J. Cell Biol 100, 2008–2018 (1985). [PubMed: 2860115]

45. Kamiya R. Extrusion and Rotation of the central-pair microtubules in detergent-treated Chlamydomonas flagella. Prog. Clin. Biol. Res 80, 169–173 (1982). [PubMed: 7100176]

46. Mitchell DR & Nakatsugawa M. Bend propagation drives central pair rotation in Chlamydomonas reinhardtii flagella. J. Cell Biol 166, 709–715 (2004). [PubMed: 15337779]

47. Omoto CK et al. Rotation of the central pair microtubules in eukaryotic flagella. Mol. Biol. Cell 10, 1–4 (1999). [PubMed: 9880321]

48. Mitchell DR Orientation of the central pair complex during flagellar bend formation in Chlamydomonas. Cell Motil. Cytoskeleton 56, 120–129 (2003). [PubMed: 14506709]

49. Wargo MJ & Smith EF Asymmetry of the central apparatus defines the location of active microtubule sliding in Chlamydomonas flagella. Proc. Natl. Acad. Sci. U.S.A 100, 137–142 (2003). [PubMed: 12518061]

50. Chen DTN, Heymann M, Fraden S, Nicastro D. & Dogic Z. ATP Consumption of Eukaryotic Flagella Measured at a Single-Cell Level. Biophys. J 109, 2562–2573 (2015). [PubMed: 26682814]

51. Zhang H. & Mitchell DR Cpc1, a Chlamydomonas central pair protein with an adenylate kinase domain. J. Cell. Sci 117, 4179–4188 (2004). [PubMed: 15292403]

52. Hou Y. et al. Chlamydomonas FAP70 is a component of the previously uncharacterized ciliary central apparatus projection C2a. J. Cell. Sci 134 (2021). doi:10.1242/jcs.258540

53. Schlauderer GJ, Proba K. & Schulz GE Structure of a mutant adenylate kinase ligated with an ATP-analogue showing domain closure over ATP. Journal of Molecular Biology 256, 223–227 (1996). [PubMed: 8594191]

54. Sekulic N, Shuvalova L, Spangenberg O, Konrad M. & Lavie A. Structural characterization of the closed conformation of mouse guanylate kinase. J. Biol. Chem 277, 30236–30243 (2002). [PubMed: 12036965]

55. Larsen TM, Wedekind JE, Rayment I. & Reed GH A carboxylate oxygen of the substrate bridges the magnesium ions at the active site of enolase: structure of the yeast enzyme complexed with the equilibrium mixture of 2-phosphoglycerate and phosphoenolpyruvate at 1.8 A resolution. Biochemistry 35, 4349–4358 (1996). [PubMed: 8605183]

56. Zhang R. et al. High-Throughput Genotyping of Green Algal Mutants Reveals Random Distribution of Mutagenic Insertion Sites and Endonucleolytic Cleavage of Transforming DNA. Plant Cell 26, 1398–1409 (2014). [PubMed: 24706510]

57. Li X. et al. An Indexed, Mapped Mutant Library Enables Reverse Genetics Studies of Biological Processes in Chlamydomonas reinhardtii. Plant Cell 28, 367–387 (2016). [PubMed: 26764374]

58. Bottier M, Thomas KA, Dutcher SK & Bayly PV How Does Cilium Length Affect Beating? Biophys. J 116, 1292–1304 (2019). [PubMed: 30878201]

59. Lin H, Kwan AL & Dutcher SK Synthesizing and salvaging NAD: lessons learned from Chlamydomonas reinhardtii. PLoS Genet. 6, e1001105 (2010).

60. Punjani A, Rubinstein JL, Fleet DJ & Brubaker MA cryoSPARC: algorithms for rapid unsupervised cryo-EM structure determination. Nat. Methods 14, 290–296 (2017). [PubMed: 28165473]

61. Zhang R, Alushin GM, Brown A. & Nogales E. Mechanistic Origin of Microtubule Dynamic Instability and Its Modulation by EB Proteins. Cell 162, 849–859 (2015). [PubMed: 26234155]

62. Lander GC et al. Appion: an integrated, database-driven pipeline to facilitate EM image processing. 166, 95–102 (2009).

63. Zivanov J. et al. New tools for automated high-resolution cryo-EM structure determination in RELION-3. elife 7, 163 (2018).

64. Pettersen EF et al. UCSF Chimera--a visualization system for exploratory research and analysis. J Comput Chem 25, 1605–1612 (2004). [PubMed: 15264254]

65. Ludtke SJ, Baldwin PR & Chiu W. EMAN: semiautomated software for high-resolution single-particle reconstructions. 128, 82–97 (1999).

66. Grigorieff N. FREALIGN: high-resolution refinement of single particle structures. 157, 117–125 (2007).

67. Sánchez-García R. et al. DeepEMhancer: a deep learning solution for cryo-EM volume post-processing. Commun Biol 4, 874–8 (2021). [PubMed: 34267316]

68. Casañal A, Lohkamp B. & Emsley P. Current developments in Coot for macromolecular model building of Electron Cryo-microscopy and Crystallographic Data. Protein Sci. 29, 1069–1078 (2020). [PubMed: 31730249]

69. Altschul SF et al. Gapped BLAST and PSI-BLAST: a new generation of protein database search programs. Nucleic Acids Res 25, 3389–3402 (1997). [PubMed: 9254694]

70. Pfab J, Phan NM & Si D. DeepTracer for fast de novo cryo-EM protein structure modeling and special studies on CoV-related complexes. Proc. Natl. Acad. Sci. U.S.A 118, (2021).

71. Brown A. et al. Tools for macromolecular model building and refinement into electron cryo-microscopy reconstructions. Acta Crystallogr. D Biol. Crystallogr 71, 136–153 (2015). [PubMed: 25615868]

72. Waterhouse A. et al. SWISS-MODEL: homology modelling of protein structures and complexes. Nucleic Acids Research 46, W296–W303 (2018). [PubMed: 29788355]

73. Zhang Y. I-TASSER server for protein 3D structure prediction. BMC Bioinformatics 9, 40 (2008). [PubMed: 18215316]

74. Song Y. et al. High-resolution comparative modeling with RosettaCM. Structure 21, 1735–1742 (2013). [PubMed: 24035711]

75. Mirdita M, Schütze K, Moriwaki Y, Heo L. & Ovchinnikov S. ColabFold-Making protein folding accessible to all. BioRxiv (2021). doi:10.1101/2021.08.15.456425

76. Afonine PV et al. Real-space refinement in PHENIX for cryo-EM and crystallography. Acta Crystallogr D Struct Biol 74, 531–544 (2018). [PubMed: 29872004]

77. Chen VB et al. MolProbity: all-atom structure validation for macromolecular crystallography. Acta Crystallogr. D Biol. Crystallogr 66, 12–21 (2010). [PubMed: 20057044]

78. Schrödinger LLC. The PyMOL Molecular Graphics System, Version 2.0.

79. Rao Q. et al. Structures of outer-arm dynein array on microtubule doublet reveal a motor coordination mechanism. Nat. Struct. Mol. Biol 28, 799–810 (2021). [PubMed: 34556869]

80. Goddard TD et al. UCSF ChimeraX: Meeting modern challenges in visualization and analysis. Protein Sci. 27, 14–25 (2018). [PubMed: 28710774]

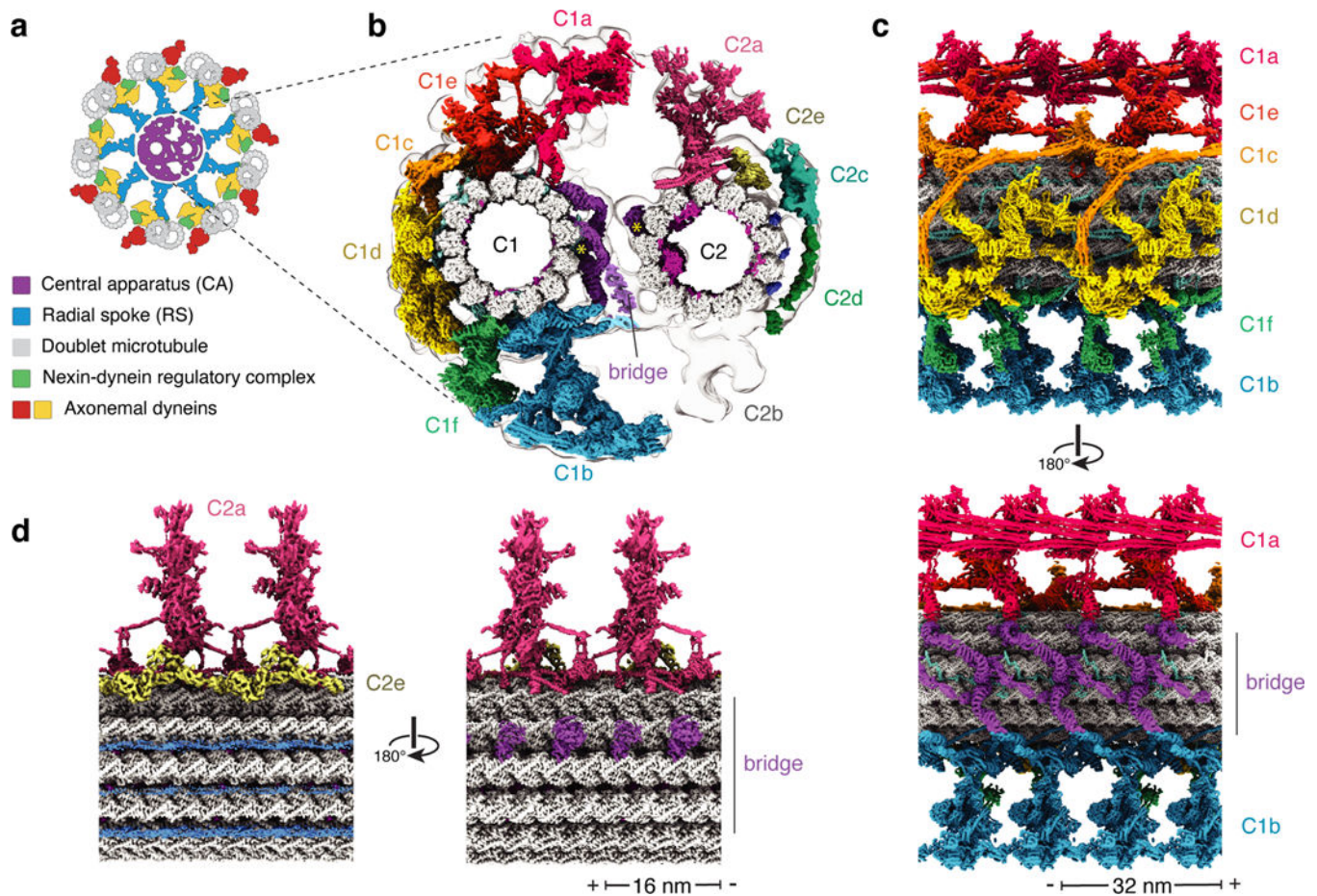81. Morin A. et al. Collaboration gets the most out of software. elife 2, e01456 (2013).

Fig. 1 |. Cryo-EM structures of central apparatus C1 and C2 microtubules.
a, Schematic representation of the cross section of the *Chlamydomonas* axoneme. The major axonemal complexes are colored and labeled. **b**, Cross section of the composite cryo-EM maps of the C1 and C2 microtubule, determined in this study, positioned within the subtomogram average of the *Chlamydomonas* CA (EMD-31143)[52]. The projections are numbered according to[5,14] and are uniquely colored. The seams of the C1 and C2 microtubules, located at the bridge, are indicated with yellow asterisks. **c**, Two longitudinal views of the C1 microtubule. **d**, Two longitudinal views of the C2 microtubule. In panels c and d, the minus (−) and plus (+) ends of the microtubules are indicated at the ends of the scale bar.
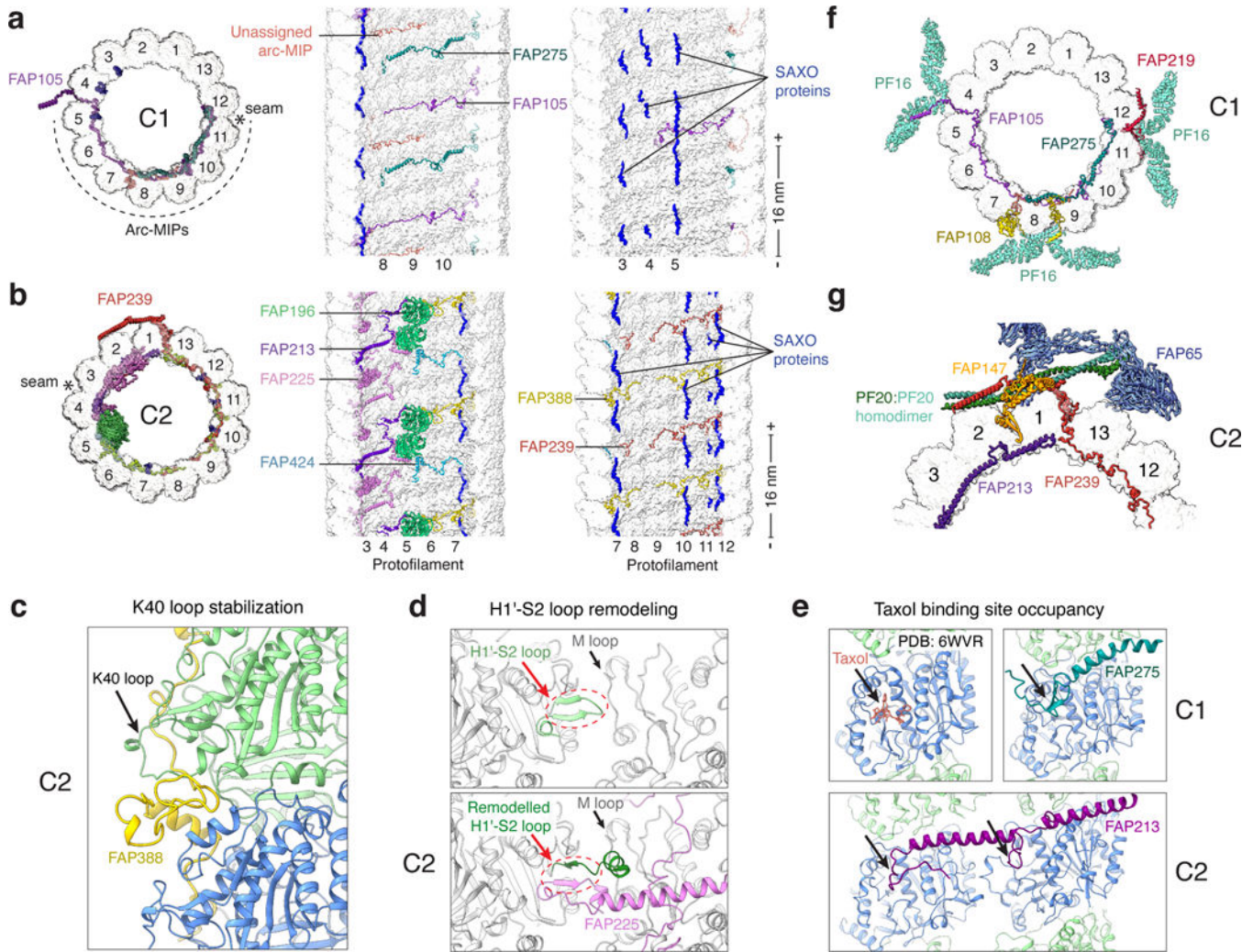
Fig. 2 |. Microtubule inner proteins (MIPs) of the central apparatus (CA).
a, Cross section (left) and two longitudinal views (middle and right) of the C1 microtubule showing the positioning and atomic models of its MIPs. **b**, Cross section (left) and two longitudinal views (middle and right) of the C2 microtubule showing the positioning and atomic models of its MIPs. In panels a and b, the minus (−) and plus (+) ends of the microtubules are indicated at the ends of the scale bar. **c**, Stabilization of the K40 loop of α-tubulin by FAP388 in the C2 microtubule. **d**, Comparison of a typical lateral interface (above) with one remodeled by FAP225 (below). FAP225 substitutes part of the H1'-S2 loop. **e**, Two examples of MIPs (FAP275 and FAP213) that insert loops into the taxol-binding pocket. In the 16-nm repeat of the C2 microtubule, 23/26 taxol-binding pockets are occupied. In the 32-nm repeat of the C1 microtubule, 14/52 are occupied. **f**, Interactions between MIPs and external proteins of the C1 microtubule. **g**, Interactions between MIPs and external proteins of the C2 microtubule. In panels f and g, MIPs are labeled within the microtubule lumen and external proteins are labeled outside the microtubule. In all panels, protofilaments are numbered according to Ref.[33].
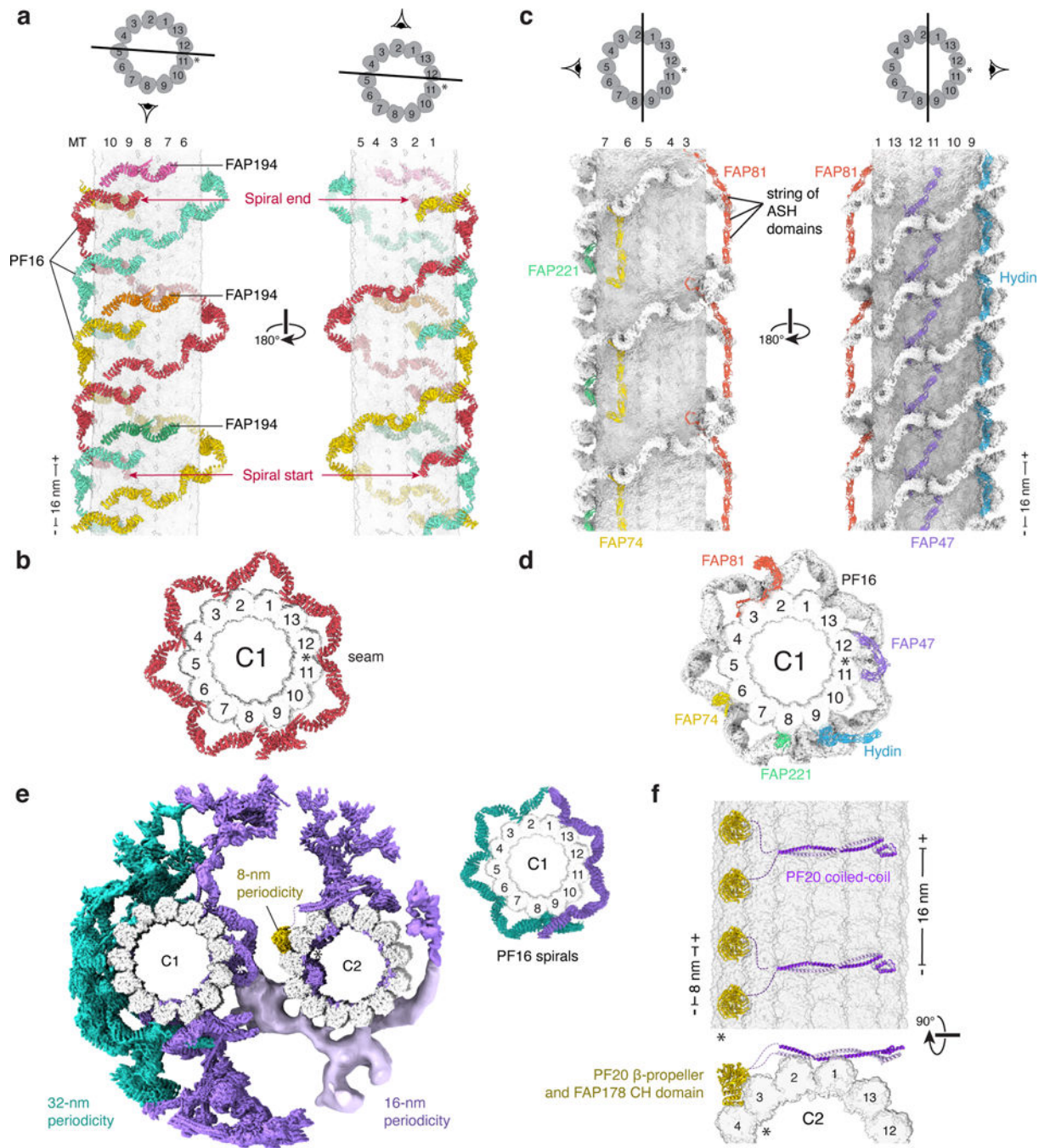
Fig. 3 |. PF16 spirals are determinants of projection asymmetry and periodicity.
a, Two longitudinal views showing how the noncontinuous spirals of PF16 form an imperfect right-handed triple helix around the C1 microtubule. Each spiral is capped after 10 homodimers of PF16 by a homodimer of FAP194. **b**, Cross section of the PF16 spirals on the C1 microtubule showing a distinctive flowerhead arrangement with a single mismatch site on protofilament 9. **c**, Two longitudinal views of the C1 microtubule showing the positions of its ASH proteins relative to the PF16 spirals. The ASH repeats form strings of domains. **d**, Positions of the ASH proteins when viewed in cross section. Each ASH protein

interacts with a specific PF16:protofilament combination. In all panels, other CA proteins are hidden for clarity. **e**, Composite cryo-EM map of the CA colored by periodicity. The map is supplemented in the C2b region with segmented density (shown in light purple) from the subtomogram average of the *Chlamydomonas* CA (EMD-31143)[52]. The pattern of periodicity of the C1 microtubule matches the periodicity of the PF16 spirals (inset). **f**, The β-propeller domain of PF20 and the calponin homology (CH) domain of FAP178 bind the seam of the C2 microtubule, following the 8-nm periodicity of tubulin. Neighboring copies of PF20 form a coiled coil at the base of the C2a projection, and thus transitions from 8- to 16-nm periodicity. The seam of the microtubule is marked with an asterisk.
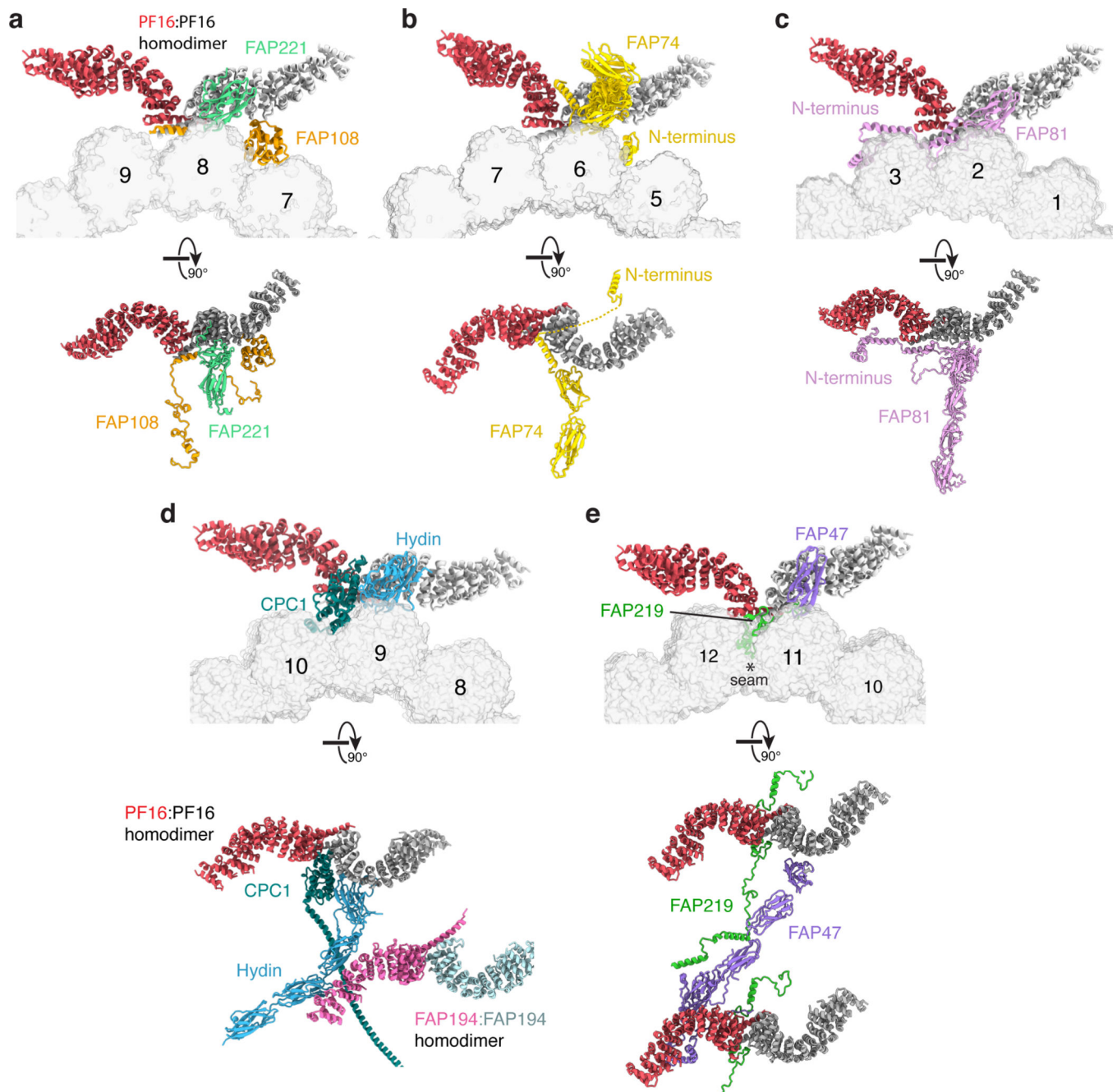
Fig. 4 |. ASH proteins recognize different PF16:protofilament combinations.
a-e, Cross sections and 90° rotations showing the binding of ASH-domain containing proteins to different PF16:protofilament combinations on the C1 microtubule. Tubulin and other microtubule-associated proteins are omitted from the longitudinal views for clarity. For FAP74 and FAP81, the interface involves contributions from their microtubule-binding N-termini. For FAP221, Hydin, and FAP47, the interface involves a third protein (FAP108, CPC1, and FAP219, respectively).
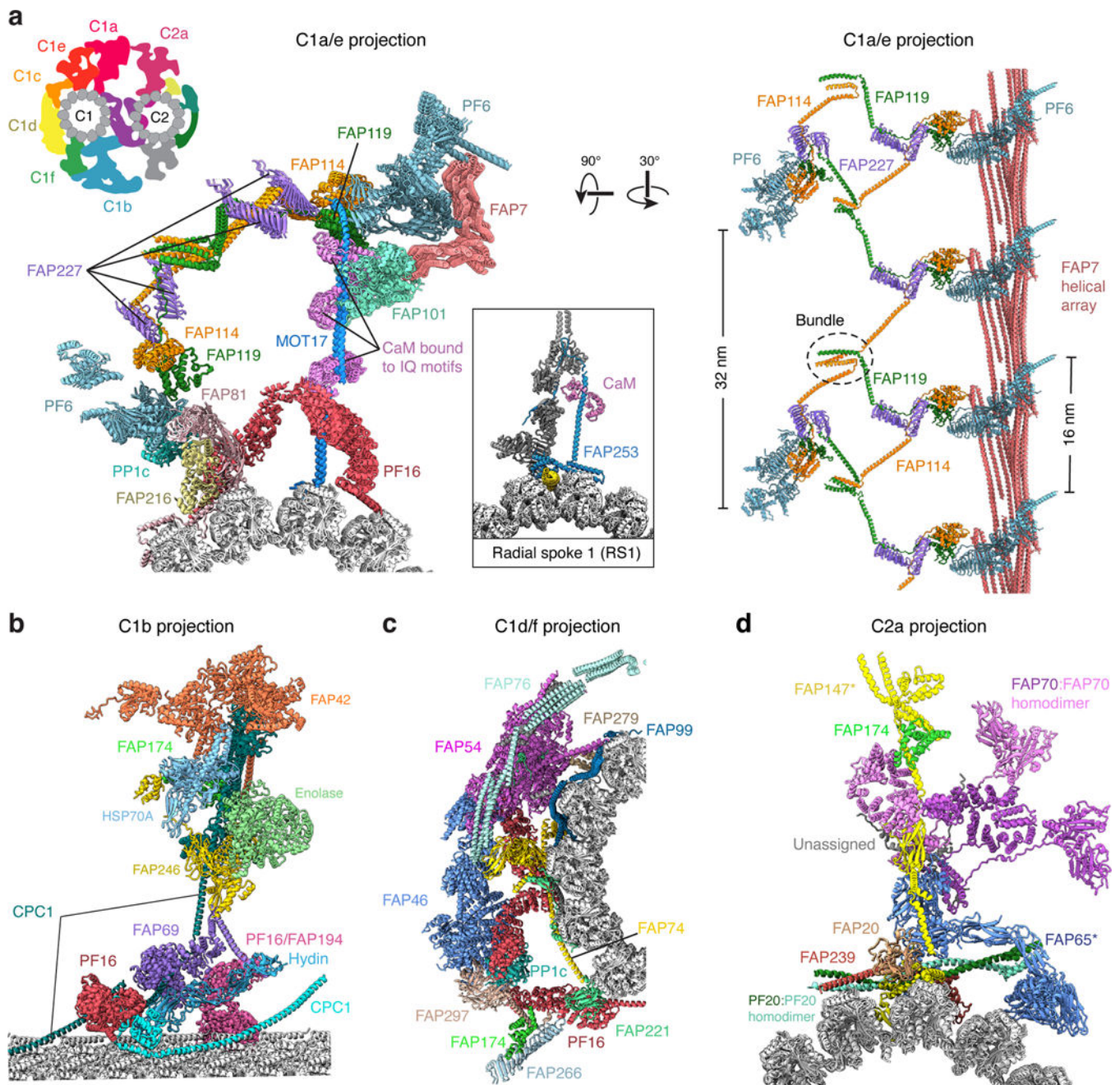
Fig. 5 |. Atomic models of the CA projections.

A schematic of the *Chlamydomonas* CA colored by projection is shown in the top left
for orientation. **a**, Domain organization of the C1a/e projection. MOT17 at the base of the
C1a projection and FAP253 at the base of radial spoke 1 (RS1; inset) both have a long
vertical α-helix that contains calmodulin-bound IQ motifs. The top view (right) shows the
helical connections between the distal regions of the C1a and C1e projections and PF6
and the FAP7 helical array that faces the C2a projection. **b**, Domain organization of the
C1b projection. Each projection contains two copies of CPC1. **c**, Domain organization of
the C1d/f projection. **d**, Domain organization of the C2a projection. The base of the C2a

projection has a coiled-coil homodimer of PF20. The stalk contains two ASH proteins (FAP65 and FAP147, highlighted with an asterisk).
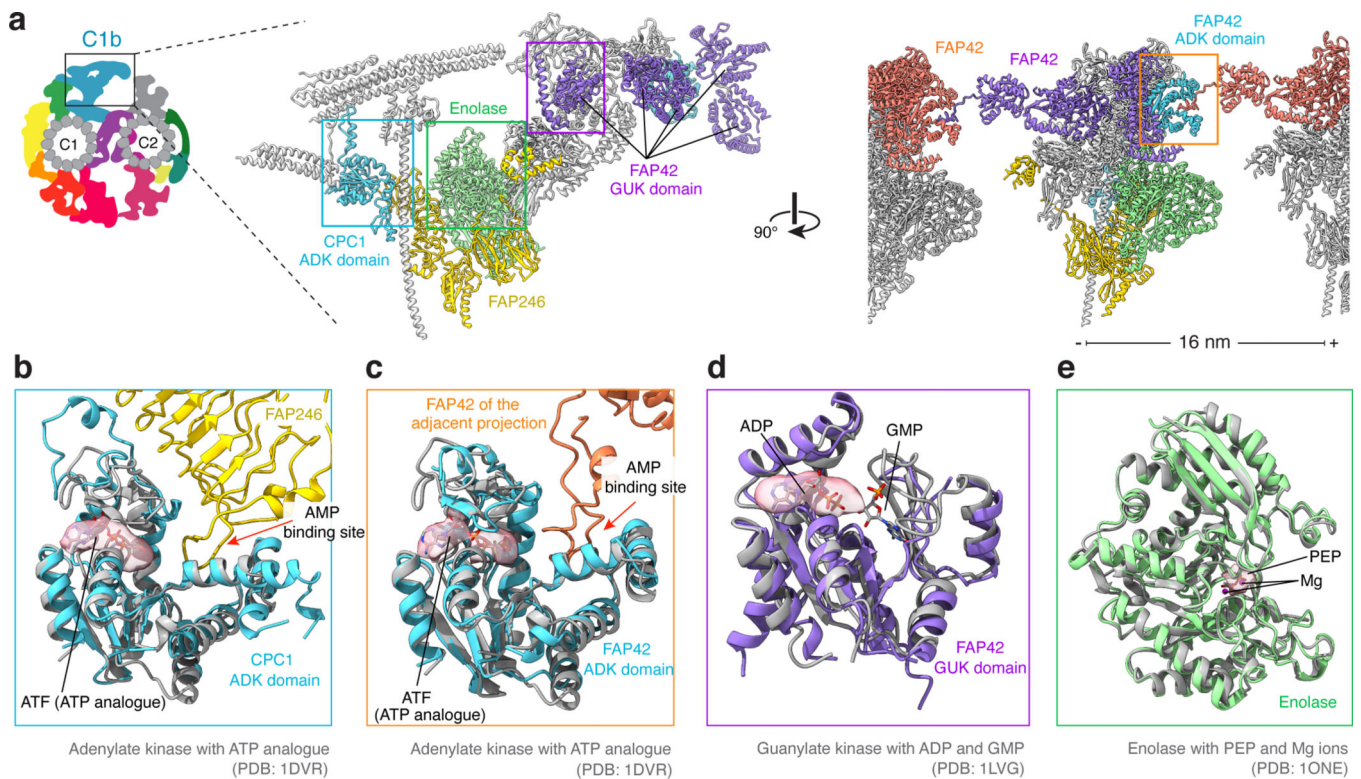
Fig. 6 |. The C1b projection contains a cluster of kinase domains.

a, Orthogonal views of the distal region of the C1b projection with a schematic of the CA cross section to aid orientation. Each C1b projection contains two adenylate kinase (ADK) domains (one each from FAP42 and CPC1), five guanylate kinase (GUK) domains from FAP42, and a homodimer of enolase. In the longitudinal view, FAP42 can be seen to interact with other copies of itself from neighboring projections. The regions boxed are shown in panels b-e. **b**, Model of the CPC1 ADK domain superposed with yeast adenylate kinase bound to an ATP analog (PDB: 1DVR) [53]. Density (transparent pink, contoured at 0.1) consistent with a nucleotide is observed in the ATP binding pocket of CPC1. The AMP binding site is occupied by a loop of FAP246. **c**, Model of the FAP42 ADK domain superposed with yeast adenylate kinase bound to an ATP analog (PDB: 1DVR) [53]. Density (transparent pink, contoured at 0.1) consistent with a nucleotide is observed in the ATP binding pocket. The AMP binding site is occupied by a loop from FAP42 of the adjacent C1b projection. **d**, Model of a FAP42 GUK domain superposed with mouse guanylate kinase in complex with ADP and GMP (PDB: 1LVG) [54]. Density (transparent pink, contoured at 0.1) consistent with a nucleotide is present in the ADP binding site. **e**, Model of an enolase monomer superposed with yeast Enolase (PDB: 1ONE) [55]. Density (transparent pink, contoured at 0.1) consistent with a small molecule is bound in the active site.

Table 1 |

Cryo-EM data collection, refinement, and validation statistics

	(1) Wild type		(2) Wild type	(3) *fap236* mutant
Data collection and processing				
Krios microscope location	WUSTL		CWRU	CWRU
Direct Detector	K2		K3	K3
Data collection software	EPU		SerialEM	SerialEM
Cs (spherical aberration) (mm)	0.01[*]		2.7	2.7
Magnification	81,000 X		64,000 X	81,000 X
Pixel size (Å)	1.39		1.34	1.07[#]
Total electron dose (e⁻/Å²)	39.6		34.0	39.3
No. of images	6,716		2,555	4,099
Defocus range (μm)	−1.0 to −3.0		−0.5 to −3.0	−0.5 to −3.0
Symmetry imposed	C1		C1	C1
C1 16-nm particle images (no.)	99,783		60,806	69,044
C2 16-nm particle images (no.)	60,241		44,565	44,321
C1 32-nm map resolution (Å)[†]		3.4–6.2		3.9–4.1[‡]
C2 16-nm map resolution (Å)[†]		3.3–5.4		3.4–3.5[‡]
FSC threshold		0.143		0.143
Refinement	**C1 microtubule PDB ID 7SQC, EMD-25381**		**C2 microtubule PDB ID 7SOM, EMD-25361**	
Model composition				
Non-hydrogen atoms	1,214,050		618,755	
Protein residues	172,262		82,184	
Ligands	97 GTP, 96 GDP, 97 Mg, 8 ANP, 4 ADP		74 GTP, 74 GDP, 74 Mg	
B factors (Å²)				
Protein	62.82		98.46	
Ligand	75.96		92.20	
R.m.s. deviations				
Bond lengths (Å)	0.006		0.003	
Bond angles (°)	0.785		0.710	
Validation				
Correlation coefficient (CCmask)	0.59		0.78	
MolProbity score	1.58		1.61	
Clashscore	6.51		6.73	
Poor rotamers (%)	0.03		0.02	
Ramachandran plot				
Favored (%)	96.58		96.38	
Allowed (%)	3.26		3.59	
Disallowed (%)	0.16		0.03	

[*] The Titan Krios microscope at WUSTL is equipped with a Cs corrector.

#The absolute pixel size was calibrated against an apoferritin structure at 2.3-Å resolution, using data collected with the Titan Krios at CWRU at 81,000 X magnification. The pixel sizes for other microscope/magnifications were calibrated accordingly using identical cryo-EM samples.

†Ranges correspond to the values of the individual maps prior to merging to form the composite map.

‡For the *fap236* mutant, we only calculated the structures for the sub-regions of the microtubule core.*fap236* represents a gene and *C1* represents a space group.